TECHNICAL DESIGN REPORT

Scientific Instrument SQS

December 2012

T. Mazza, H. Zhang, and M. Meyer
for Scientific Instrument SQS (WP85)
at the European XFEL

European
XFEL

Contents

1   Introduction

This document represents the technical design report for the Small Quantum Systems (SQS) scientific instrument at the European XFEL (referred to as "SQS-TDR_2012" in the following text). It provides the technical specifications and design studies for the experiment station and its equipment, including the layout of the focusing optics for the free-electron laser (FEL) beam. SQS-TDR_2012 is based on the conceptual design report for the SQS scientific instrument (SQS-CDR), which was released in 2011 and which is accessible on the website of the European XFEL:

https://www.xfel.eu/research/instruments/sqs

Since the installation of the end station in the experiment hall is scheduled to start in mid-2015 and the commissioning of the SQS instrument will start at the earliest in the beginning of 2016, it is clear that the specification of some components might be revised later in view of the latest developments. In particular, the enhancement in the performances of optical and electronic equipment as well as the progress in detector technology are presently quite significant and fast. The final realization of the SQS instrument will have to include these latest technical advances and improvements in order to provide optimal experimental conditions with state-of-the-art equipment to the user community. In this respect, the present document describes the current status of the technical design for the SQS instrument rather than the compilation of the final parameters. Nonetheless, it is the primary basis for all further discussions and studies aiming to improve the performances of the SQS instrument.

The report first presents the SASE3 beamline (Chapter 2), including a short reminder of the main parameters of the European XFEL in the soft X-ray regime (Section 2.1), the layout of the beamline (Section 2.2), and the description of the soft X-ray monochromator (Section 2.3). The main part of the document (Chapter 3) is devoted to the description of the technical design of the SQS instrument, presenting first the floor plan of the experiment area of

the SQS end station (Section 3.1) and then placing specific emphasis on the Kirkpatrick-Baez (KB) focusing optics (Section 3.2) and the atomic-like quantum systems (AQS) and the nano-size quantum systems (NQS) experiment chambers (Section 3.3). The data acquisition and experiment control systems are discussed in Chapter 4. Thereafter, the present status for the sample delivery systems (Chapter 5), the optical laser equipment at the SQS experiment station (Chapter 6), add-on equipment (Chapter 7), and FEL beam diagnostics (Chapter 8) are outlined. At the end, a possible timeline for the installation of the equipment is sketched (Chapter 9).

2 SASE3 beamline

2.1 Parameters for the soft X-ray regime

The electron bunches in the linear accelerator are deviated about 2 km behind the electron source into two branches, which accommodate the SASE1 and SASE2 hard X-ray undulators, respectively (Figure 2.1). The soft X-ray undulator SASE3 is located 0.5 km upstream behind SASE1. This undulator represents the source point for the FEL radiation dedicated to experiments at the scientific instruments SQS (Small Quantum Systems) and SCS (Spectroscopy and Coherent Scattering), which are installed about 450 m behind the SASE3 undulator in the experiment hall of the European XFEL facility.
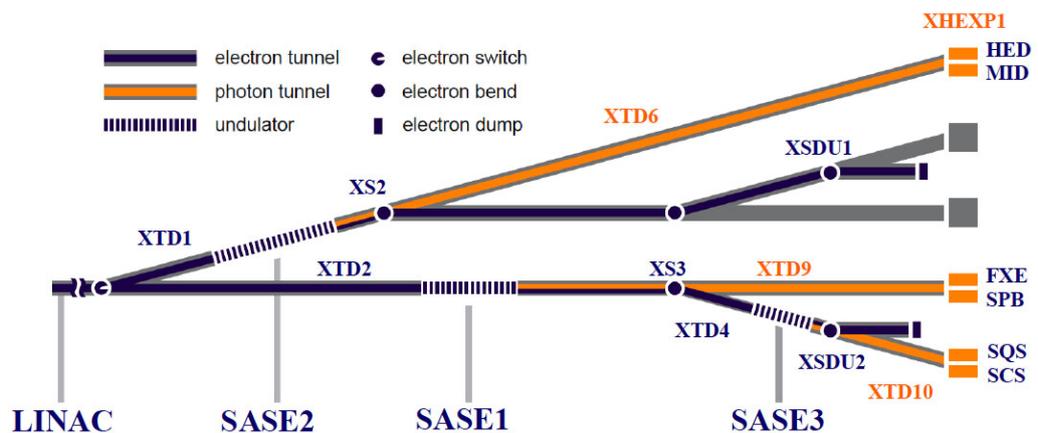
Figure 2.1: Electron and photon beam distribution for the European XFEL

The linear accelerator will operate at three different energies for the electron beam, namely 10.5, 14 and 17.5 GeV. The resulting photon energy range for the undulators SASE1, SASE2, and SASE3 is schematically shown in Figure 2.2. The lowest photon energy accessible for experiments at SASE3 is 260 eV (4.8 nm), which is reached only in the 10.5 GeV operation mode. For higher electron energies, the minimal photon energy shifts to 470 eV (14 GeV) and 730 eV (17.5 GeV). The high-energy limit for the XUV radiation

is mainly determined by the reflectivity of the optics in the beamline and can reach up to 4 keV.
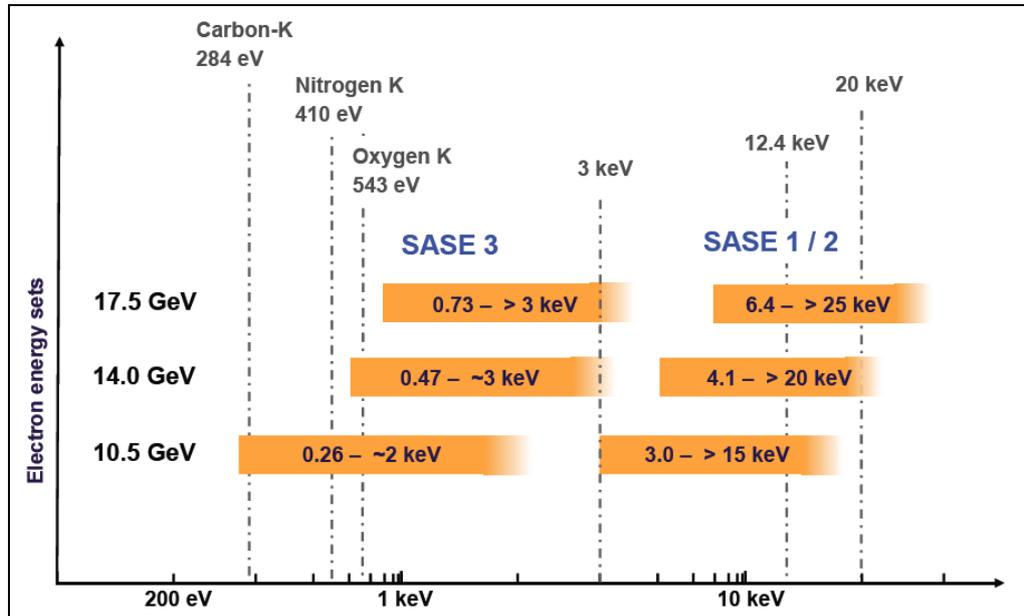
Figure 2.2: *Photon energy range available for the SASE1, SASE2, and SASE3 undulators for the different operation modes of the accelerator*

All other principal FEL beam parameters of the SASE3 undulator are summarized in Table 2.1. On the one hand, pulse durations as short as 2 fs are available in the low-charge mode (20 pC) enabling e.g. time-resolved studies in the few-femtosecond time domain. On the other hand, pulse energies of up to 10 mJ are produced at high bunch charges (1 nC). This high pulse energy corresponds to 2×10^{14} photons per pulse and is the main requirement for the study of non-linear processes, since intensities of more than 10^{18} W/cm^2 can be reached by focusing e.g. the 10 mJ / 100 fs FEL beam to a diameter of about 1 μm.

Table 2.1: Soft X-ray (SASE3) FEL parameters for selected settings of the electron energy and bunch charge [from Tschentscher (ed.), XFEL.EU TN-2011-001, (2011)]

Photon energy	keV	0.28			0.496			1.55			3.1		
Wavelength	nm	4.43			2.5			0.8			0.4		
Electron energy	GeV	10.5			14			14			14		
Bunch charge	nC	0.2	0.25	1	0.2	0.25	1	0.2	0.25	1	0.2	0.25	1
Peak power	GW	105	106	94	118	119	105	90	86	72	73	66	51
Average power	W	5	67	273	5	75	304	4	54	209	3	41	147
Source size (FWHM)	μm	51	65	79	43	56	68	39	50	60	36	46	56
Divergence (FWHM)	μrad	33.9	29.6	26.0	23.1	20.0	17.5	9.7	8.1	6.9	5.6	4.6	3.9
Spectral bandwidth	1E-3	6.9	6.4	5.7	5.8	5.3	4.7	4.4	3.9	3.3	3.6	3.1	2.5
Pulse duration	fs	2	23	107	2	23	107	2	23	107	2	23	107
Coherence time	fs	1.49	1.63	1.83	1.01	1.11	1.25	0.43	0.49	0.57	0.26	0.31	0.38
Coherence degree		0.96	0.96	0.96	0.96	0.96	0.96	0.96	0.96	0.96	0.96	0.96	0.91
Photons / pulse	1E11	39	547	2240	25	347	1420	6	81	312	2	31	109
Pulse energy	mJ	0.2	2.5	10.1	0.2	2.8	11.3	0.2	2.0	7.8	0.1	1.5	5.4
Peak brilliance	1E31	7	7	7	16	17	17	49	54	53	98	104	93
Average brilliance	1E21	3	46	212	7	109	498	22	338	1520	44	654	2680

The primary advantage of the European XFEL over other X-ray free-electron laser sources (LCLS, SACLA, Swiss-FEL) is the extremely high number of light pulses (maximum 27 000 pulses per second) and therefore the high average brilliance, which can be used for experiments. The FEL pulses are produced in bunch trains with a repetition rate of 10 Hz. Each train is 600 μs wide and contains 2700 individual pulses (Figure 2.3). The nominal temporal separation between the individual pulses within a bunch train is set to 220 ns (4.5 MHz). As a consequence, the design of the scientific instruments will place emphasis on experimental techniques taking advantage of or/and requiring this high number of pulses. One possible operation mode for the experiments would provide about 1250 bunches per train, since the electron bunches are split into the two branches for SASE1/SASE3 and SASE2, respectively, in order to allow parallel operation of all instruments. Other operation modes are possible, but have to be integrated in the overall coordination of experiments at the different end stations. In addition, different bunch separation patterns are possible (N x 220 ns, including unequal spacing within a pulse train), and inter-pulse periods in the microsecond range (0.1–0.9 MHz) down to single-bunch operation (10 Hz) can be provided.
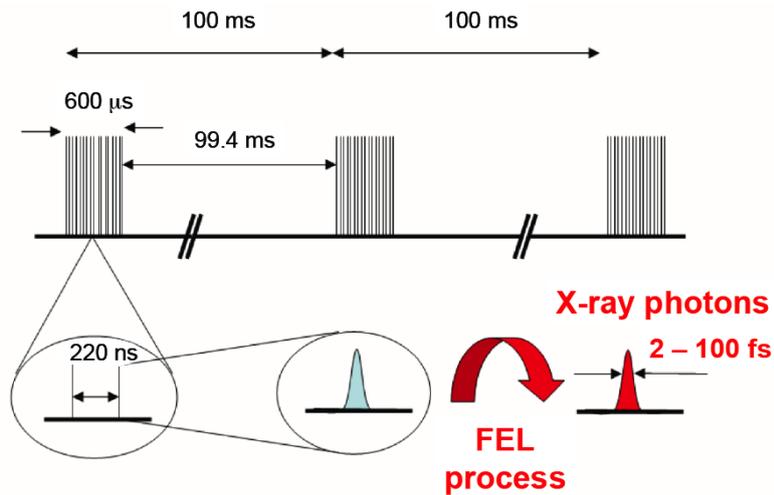
Figure 2.3: Pulse structure for the operation mode of the European XFEL

In addition, options for using variable polarization, i.e. linearly and circularly polarized XUV light, as well as the possibility for self-seeding in the XUV regime are under consideration. These options are not further discussed in this TDR. The use of these beam characteristics integrates without difficulty into the present design of the instrumentation for the SQS scientific instrument, even enhancing the performances of the experiment station.

2.2 Layout of SASE3 beamline

The photon beam transport and the layout of the SASE3 beamline are discussed in the technical design report dedicated to the beam transport system [H. Sinn, TDR-BT_2012]. A schematic overview of the devices, which are installed in the 418.5 m long tunnel section between the SASE3 undulator and the experiment hall, is given in Figure 2.4.
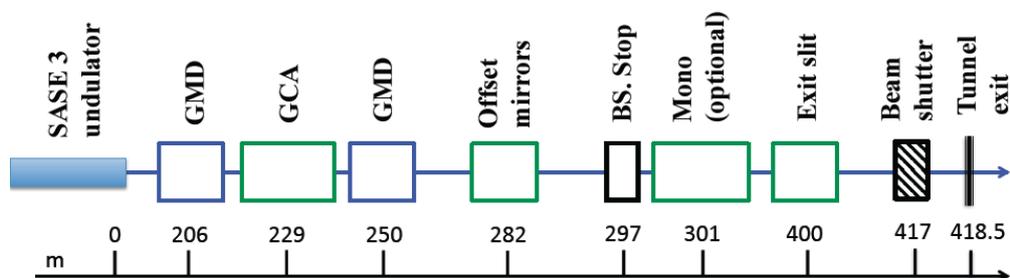

Figure 2.4: Schematic presentation of the main components for the SASE3 beamline

The most relevant components are the following items:

- **Soft X-ray monochromator** ("Mono"). The monochromator serves mainly for the SCS instrument, but can also be used for experiments at the SQS instrument and the open port. More details are given in the next section.

- **Offset mirrors** protect the experiment area against high-energy radiation and, at the same time, act also as filter for higher-order radiation. The incidence angles can be varied in the range 6–20 mrad (instead of 9–25 mrad as given in SQS-CDR). The main reason is the smaller wavefront distortion coming from shape errors of the mirrors. In addition, due to the smaller possible angle, the SQS experiment could now receive beam with photon energies up to nearly 4 keV. The mirrors are 800 mm long and equipped with a cooling system to minimize deformation of the surface due to the high integrated beam power, which can reach 100 W for the first mirror.

- **Intensity monitors (gas monitor detector, GMD)** provide an online measurement of the FEL intensity. Two of these devices are located around the gas absorber. A detailed description of the GMD is given in Chapter 6 dedicated to the FEL beam diagnostics.

- **Gas cell attenuator (GCA)**. This gas cell enables the user to vary in a controlled and accurate way the intensity of the XUV radiation by three orders of magnitude or more depending on the photon energy and the used gas. The GCA provides the possibility to investigate the intensity dependence of physical processes, in particular non-linear phenomena, over a large interval without modifying the undulator configuration.

The complete GCA has a total length of about 32.5 m including the 15 m long gas cell and differential pumping stages on each side of the cell (Figure 2.5). A set of turbo pumps and an additional triode ion pump on each side ensure a vacuum of less than 5×10^{-7} mbar outside the high-pressure absorption cell despite the large apertures of 25 mm. The size of the apertures is defined by the large beam diameter of the XUV radiation.
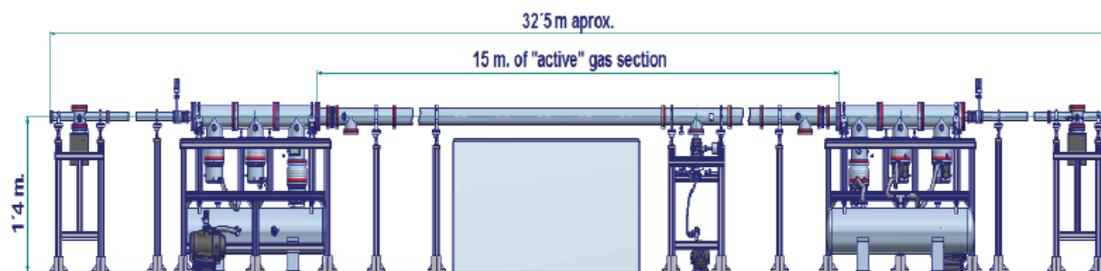
Figure 2.5: Schematic view of the gas cell attenuator on the SASE3 beamline [TDR-BT_2012]

The principal "working" gas is nitrogen. However, to expand the range of applications of the GCA (i.e. avoiding the "discontinuity" produced by the absorption peak of nitrogen around 400 eV or being able to achieve higher levels of attenuation, etc.), some alternative noble gases (Xe, Ne, Kr and Ar) have been also included in the design.

Table 2.2 summarizes the main features of the GCA.

Table 2.2: Main characteristics of the GCA [TDR-BT_2012]

Parameter	Value
Attenuation path	15 m
Working gas	N_2
Working gas pressure range	10^{-4} to 15 mbar
Max. attenuation ($I_0{:}I$)	Up to 3 orders of magnitude
Admissible range of beam energy to achieve maximal attenuation	260 eV to 3.5 keV

2.3   Soft X-ray monochromator

The SQS scientific instrument makes preferential use of the direct non-monochromatized FEL beam, i.e. focuses on applications requiring the highest intensity and/or highest available temporal resolution. For specific applications, it is also possible to perform experiments under high spectral resolution, i.e. using the FEL radiation after the soft X-ray monochromator in

the SASE3 beamline. The monochromator is installed about 20 m behind the offset mirrors. The general layout of all optical elements, which are installed in the tunnel before the experiment area, is given in Figure 2.6.
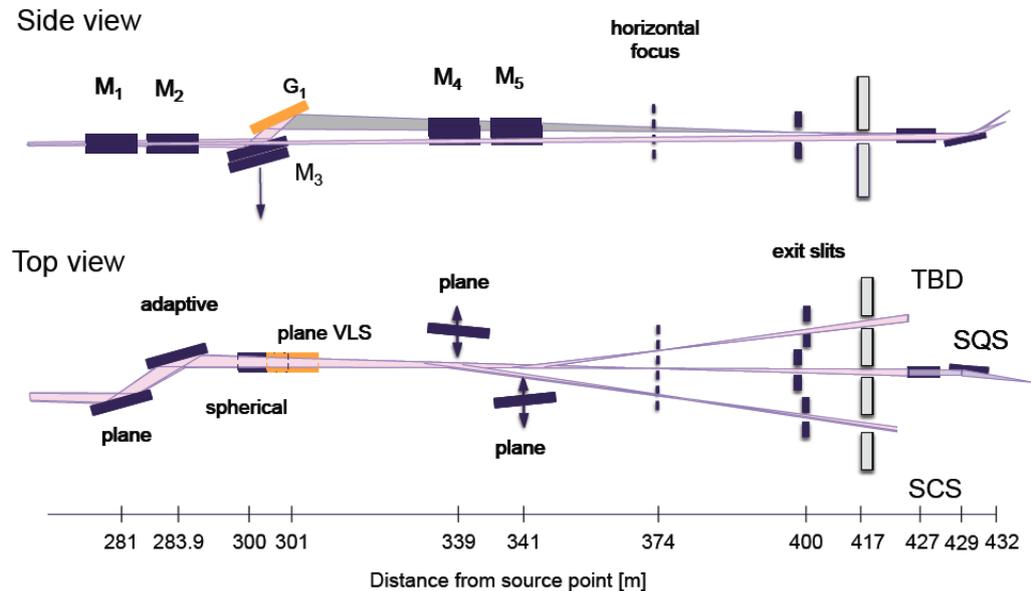

Figure 2.6: *Schematic layout of the SASE3 beamline including the VLS monochromator [from TDR-BT_2012]*

The optical design of the soft X-ray monochromator is based on the variable line spacing plane grating monochromator (VLS-PGM) scheme. The energy scan is performed by the VLS grating rotation at fixed incidence angle. The monochromator is designed to cover the energy range from 270 to 3000 eV. As an option, operation with the non-monochromatized beam (pink beam) is also possible in this configuration. Through insertion of a plane mirror about 40 m behind the VLS grating, the beam can be steered to the two side branches, i.e. to the SCS scientific instrument and the open port (SQS/SCS-2, labelled "TBD" in Figure 2.6), respectively.

Remote-controlled manipulators enable the alternate insertion into the beam of one of the two cylindrically shaped pre-mirrors. Each pre-mirror is optimized for a specific energy range and both mirrors focus the beam vertically on the exit slit. The pre-mirror deflects the beam on the plane VLS grating. Two gratings with different line density (50 and 150 l/mm) are comprised in the design in order to reach a spectral resolution $\lambda/\delta\lambda$ of more than 10^4 over the whole energy range (Figure 2.7). A blank mirror (without

ruling) is mounted together with the gratings for calibration purposes and can also reflect the vertically focused pink beam. Both the pre-mirrors and the grating have to be water-cooled to ensure the achievement of the final performance.
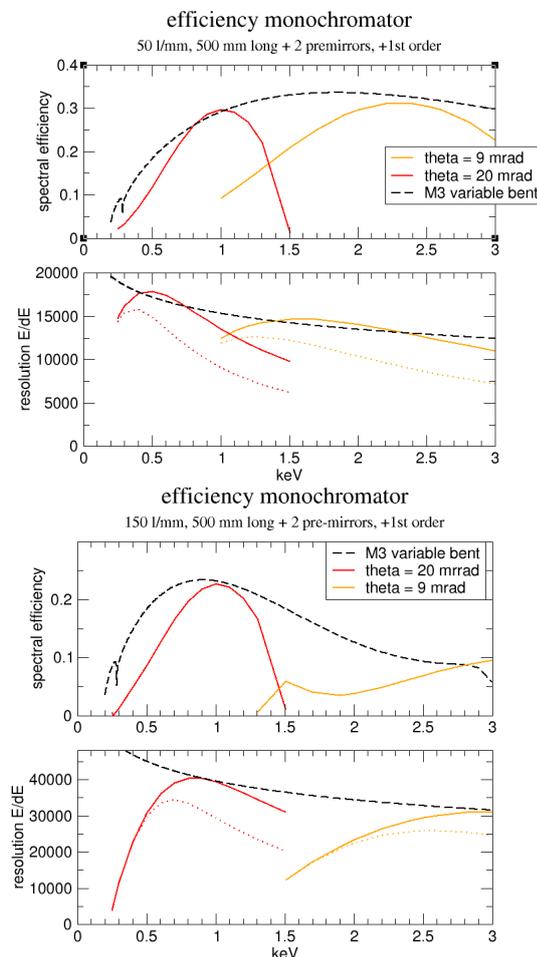
Figure 2.7: Top panel: *Spectral efficiency according to scalar approximation.* Lower panel: *Estimation of resolution (source size is assumed 60 (dotted line: 100) µm FWHM). The grating depth is 15 nm. [TDR-BT_2012]*

A direct consequence of increasing the spectral resolution by a grating is the temporal broadening of the FEL pulses. When using e.g. the highest resolution (40000) of the 150 l/mm grating at 1000 eV photon energy (Figure 2.8), the pulses are stretched to about 200 fs.
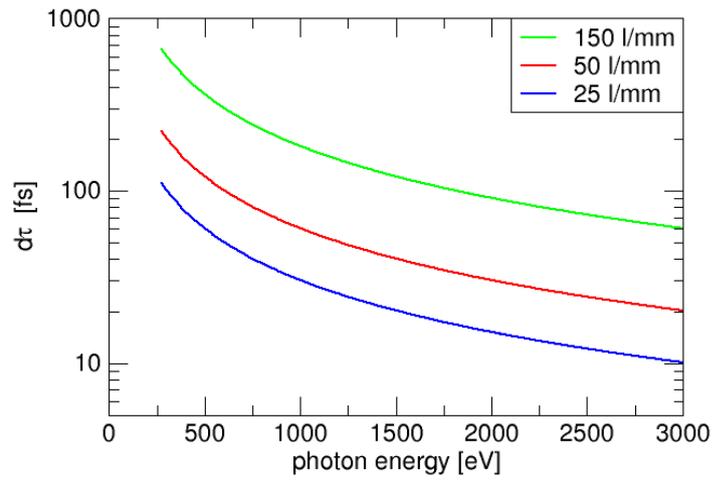
Figure 2.8: *Pulse stretching for a 4-sigma illuminated grating of 500 mm length [TDR-BT_2012]*

3 SQS scientific instrument

3.1 SQS experiment area

In the experiment hall, an area of about 650 m^2 is dedicated to the installation of the experiment stations that are using the intense soft X-ray radiation produced by the SASE3 undulator (Figure 3.1.1). The maximal length is 42.5 m and the overall width of the area amounts to 15.5 m. The SQS scientific instrument is installed on the central beamline at the end of the experiment area. The two beamlines on the side branches delivering the beam to the SCS instrument and to the (not yet defined) open port, labelled SQS/SCS-2, are installed under an angle of 18 mrad with respect to the central branch, which results in a horizontal separation of 1.421 and 1.341 m, respectively, at the exit of the tunnel. In addition to the experiments, space is allocated to host the optical laser system used for two-colour pump–probe (PP) experiments.
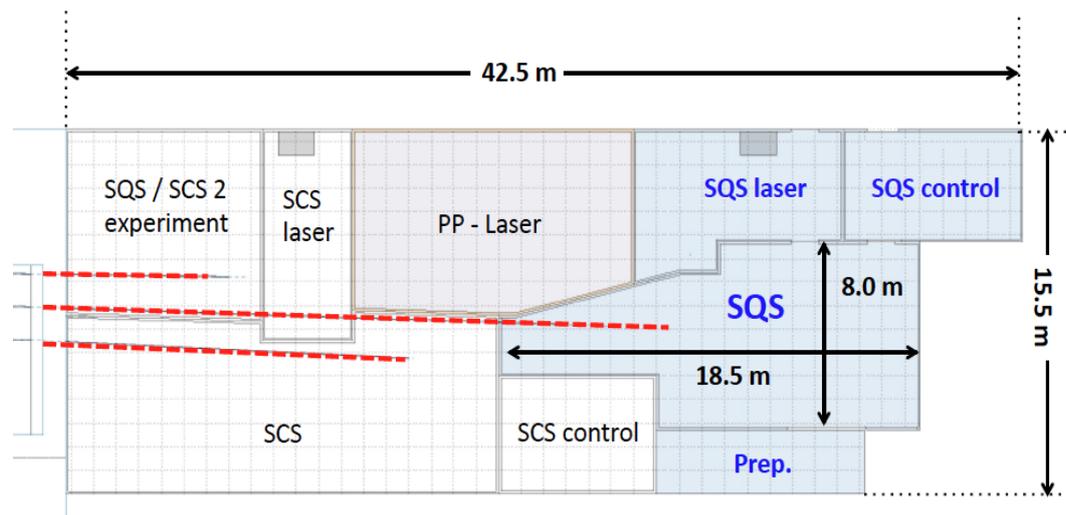
Figure 3.1.1: Layout of the SQS experiment area, the control room, and the preparation area on the floor space behind the SASE3 undulator

Both scientific instruments, SQS and SCS, are built up on a surface of about 200 m^2 each. For the SQS/SCS-2 experiment and for the optical laser hutch, including the pump–probe laser, beam distribution system, and delay line, an area of about 90 m^2 each is reserved on the experiment floor.

Based on a recent study performed by Y. Asano (SACLA) in July 2012 and dedicated to the radiation safety requirements in the experiment hall of the European XFEL, the experiment area for the SQS instrument has to be shielded by 0.3 mm (side walls) to 5 mm (wall at the end) thick iron plates and a 3 x 300 x 300 mm^3 lead plate (behind the beam stop). This safety hutch (Figure 3.1.2) will equally fulfil the safety requirements for handling the optical laser. As a consequence, limited access to the experiment area of the SQS instrument might be given during FEL beam operation in the central beamline. In order to enable specific preparation and characterization of the optical laser beam also during FEL operation, the area including two optical tables will therefore be separated from the experiment area and will be accessible independently. The experiment area can be accessed directly from the walkway as well as from the control room. A large double door is installed close to the elevator to enable installation and exchange of large equipment.
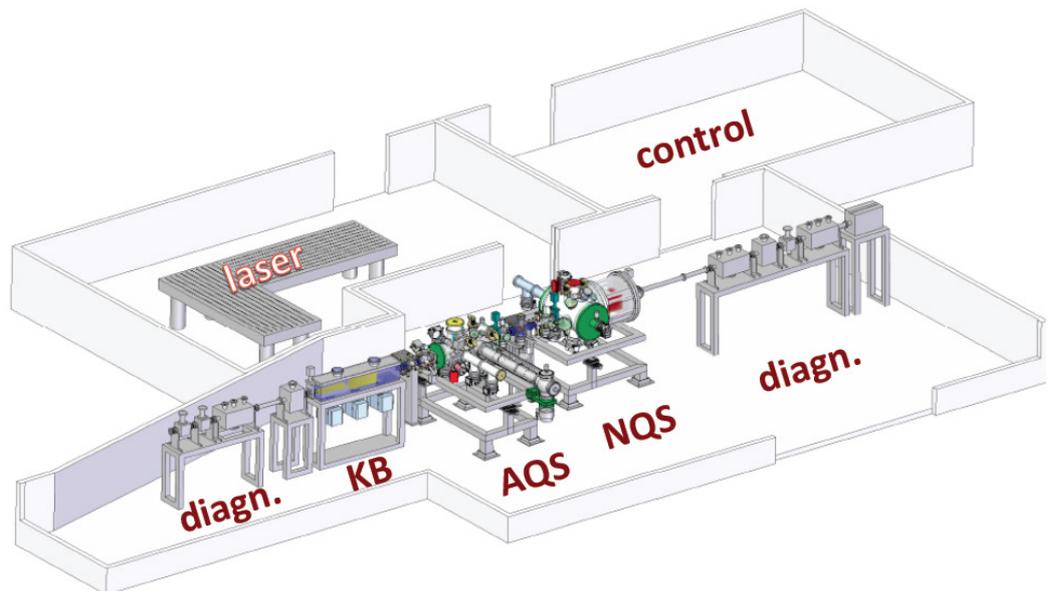
Figure 3.1.2: *Layout of the SQS experiment area with the control room and SQS laser hutch*

A total height of about 4.5 m is envisaged, which provides enough space for the installation of an additional crane inside the experiment hutch. The crane enables the mounting and exchange of heavy equipment, such as spectrometers, pumps and detectors, on the vacuum chambers as well as the displacement of the chambers and diagnostic units.

Additional space is available outside the shielded area for the control of the experiments performed at the SQS experiment station (about 30 m^2) as well as for the preparation of experimental equipment (about 25 m^2) that is not requiring the FEL beam.

In the SQS experiment area, which has a total length of 18.5 m, a large number of items will be installed along the beamline (Figure 3.1.3). The most relevant items, which are discussed individually in the subsequent sections, are the following:

1   Experiment station including the AQS and NQS chambers

2   Kirkpatrick-Baez (KB) focusing optics

3   Dedicated optical laser system

4   FEL beam diagnostics

5   Beam stop
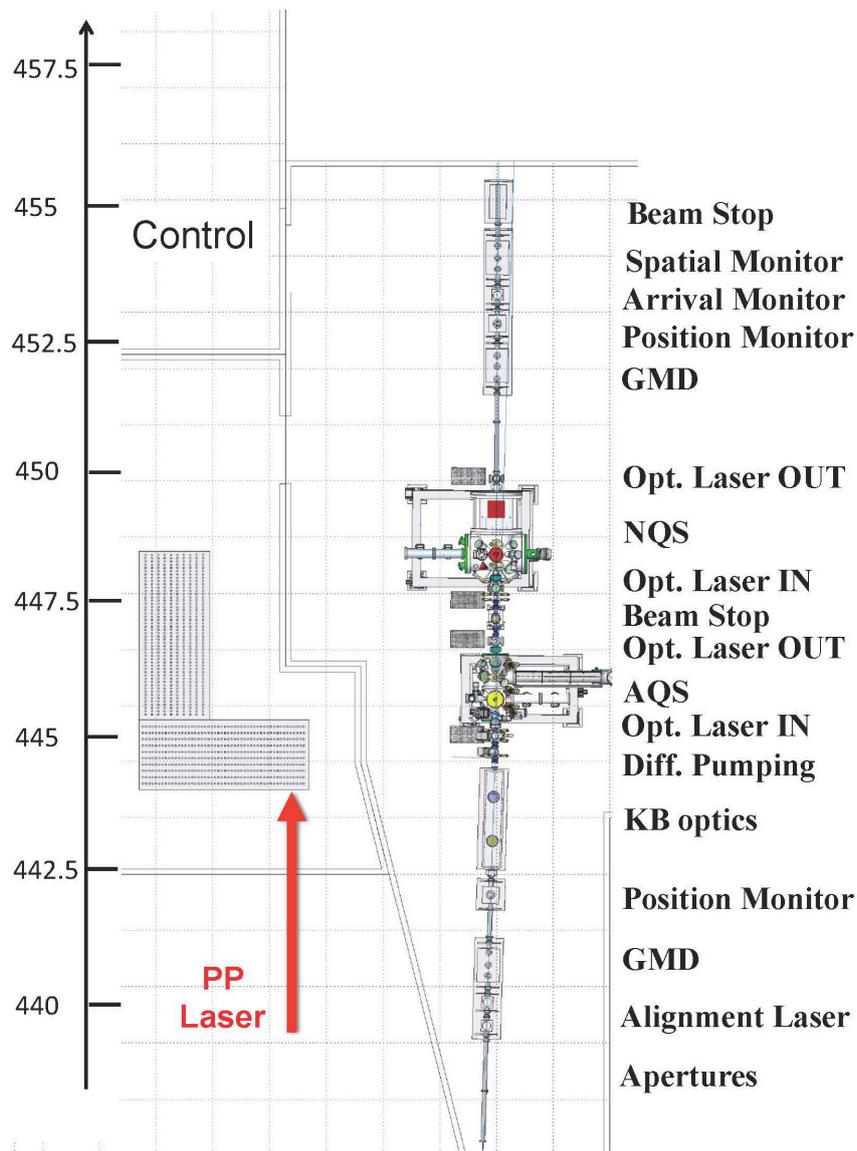
Figure 3.1.3: *Schematic view of all components used in the SQS experiment area*

The experiment station (Figure 3.1.4) consists of two separate vacuum chambers, AQS and NQS, which are mounted at a distance of about 445 and 447 m, respectively, from the SASE3 undulator, or 27 and 29 m from the exit of the undulator tunnel. These two chambers are dedicated primarily to different sample types, atomic-like quantum systems (AQS) and nano-size quantum systems (NQS), but the specific instrumentation of each chamber also reflects differences with respect to the principal experimental methods, i.e. high-resolution studies and coincidence spectroscopy for AQS, and diffraction imaging experiments and coincidence spectroscopy for NQS. Both chambers are equipped with independent sample delivery and pumping

systems, diagnostics, and alignment tools. An optional beam stop can be introduced between both chambers.
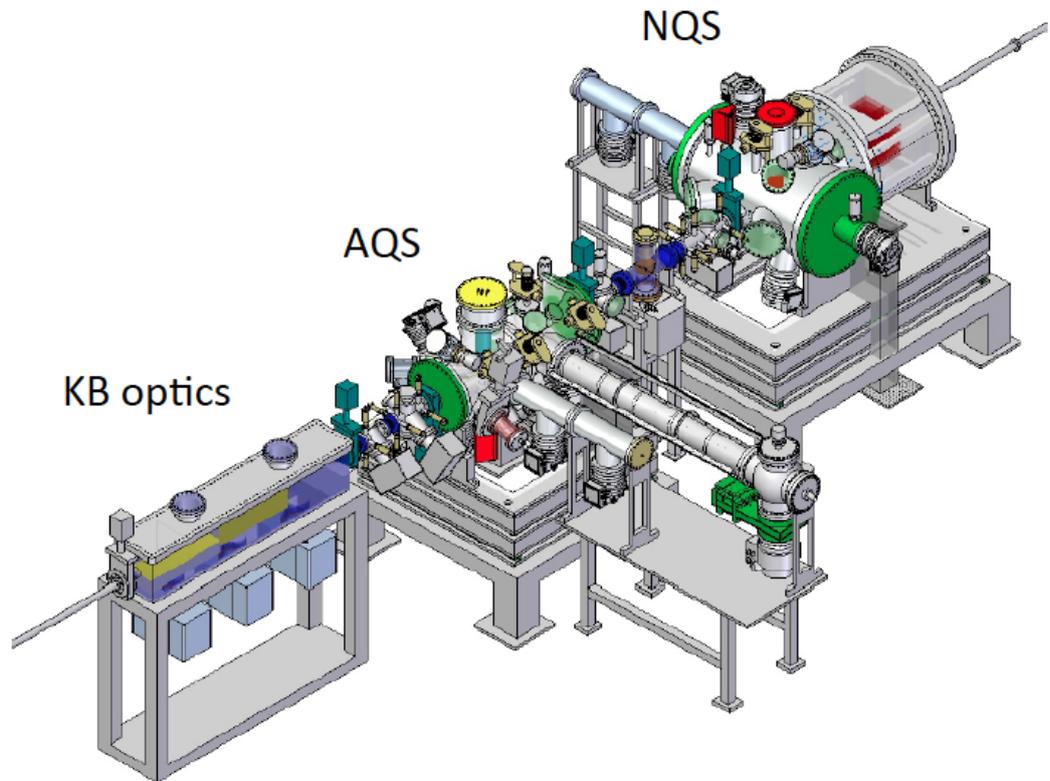
Figure 3.1.4: *Global view of the SQS experiment station with the AQS and NQS vacuum chambers and the KB focusing optics*

The focusing optics provides three focal points along the beam propagation direction: F1 and F1' in the AQS chamber, and F2 in the NQS chamber (Figure 3.1.5). The separation between the two principal interaction points (F1 and F2) is mainly determined by the length of the AQS chamber, comprising two interaction points, the installation of the in- and out-coupling unit for the optical laser, and the space required to install an intermediate beam stop between the AQS and NQS chambers. Based on these constraints, the distance between F1' and F2 is set to 2.188 m.

The distance between the KB mirror chamber (centre of the last, horizontal focusing mirror, HFM) and the AQS chamber is determined to a large degree by the vacuum requirements of the AQS chamber (10^{-11} mbar) with respect to those of the KB mirror chamber (10^{-9} mbar). In addition, an in-coupling unit for the optical laser is foreseen to enable two-colour experiments in collinear

geometry. The shortest distance between the centre of the HFM and the focal point F1' is therefore set to 2.00 m. The first focus (F1) of the AQS chamber lies 39 cm upstream.
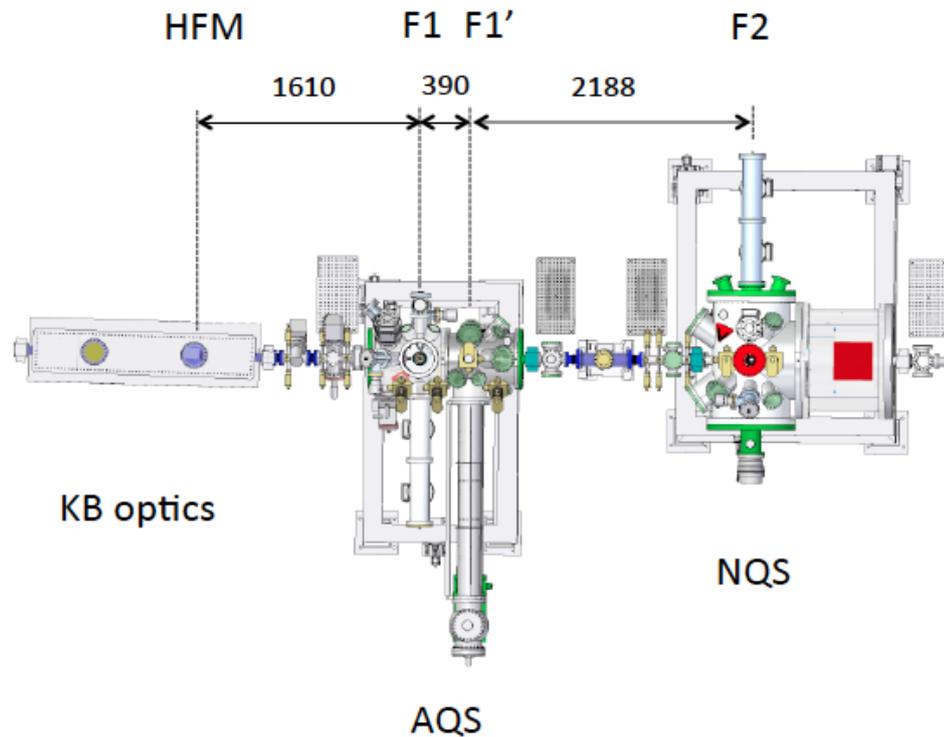

Figure 3.1.5: Top view of the SQS experiment station with the AQS and NQS vacuum chambers and the KB focusing optics

The beam height is 1.40 m at the entrance of the KB mirror chamber and 5.2 (10.9) cm higher at the position of the AQS (NQS) interaction point.

Both chambers are built in a modular way, i.e. similar standards are used wherever possible in order to facilitate easy exchange of equipment (spectrometers) between both chambers, including the large imaging detector.

In addition, the layout of the whole instrument and the space available around the AQS and NQS chambers will also allow, if necessary, the exchange of both chambers, enabling imaging experiments in the smallest available focus of the XUV beam. The chosen distances for the focus positions (F1 and F2) also match when the order of installation of the AQS and NQS experiment chambers is inverted (Figure 3.1.6).
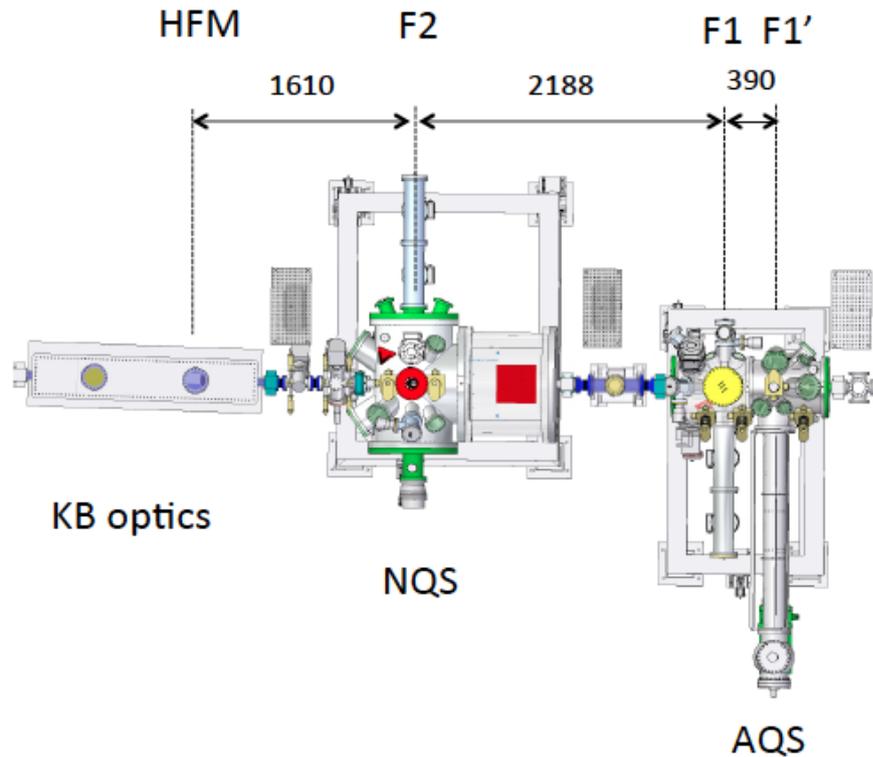
Figure 3.1.6: Top view of the SQS experiment station with the NQS and AQS vacuum chambers and the KB focusing optics. The order of the AQS and NQS chamber is inverted with respect to the configuration shown in Figure 3.1.5.

3.2   KB focusing optics

The present section specifies the characteristics of the Kirkpatrick-Baez (KB) mirror system, which will be installed at the central beamline of SASE3 defining the focus conditions for experiments at the SQS instrument. A KB system is the only feasible solution in the soft X-ray wavelength regime to provide the required minimal focus diameter of about 1 μm (or less) in the interaction region while maintaining a high intensity.

The design of the KB system is optimized taking into account the following requirements:

■ Enable high transmission of the photon beam over the entire photon energy range of SASE3 (250–3000 eV);

- Provide < 1 μm focusing conditions in three different points along the beam propagation axis (see Section 3.1). The distances of the interaction points from the exit flange of the KB mirror chamber are:

  — F1 (AQS):   1230 mm

  — F1' (AQS):   1620 mm

  — F2 (NQS):   3808 mm

- Allow tuning of the spot size from the minimum value (≤ 1 μm) to larger diameters of 10, 20, or 50 μm, as required by experiments where non-linear effects in the X-ray regime must be avoided;

- Allow steering of the beam coming from both the undulator and the exit slit of the monochromator to enable pink-beam and monochromatic-beam operation of the instrument.

The performances in transmission, focusing power, and focusing dynamic range as well as the technical feasibility of a KB mirror system are determined by a number of specifications:

- Mirror coating material, determining reflectivity;

- Incidence angle, determining reflectivity and aperture and affecting the mirror profile;

- Mirror length, determining aperture and affecting pointing stability;

- Ratio between source and image distance, determining the focusing power and affecting the mirror profile;

- Surface error, determining the focusing power.

The search for an optimal configuration within this parameter space is significantly complicated by the broad range of working conditions defined by the instrument design, requiring quite different optimal settings, which might even be incompatible with each other. The relatively high number of different working conditions (3 working positions x 4 focus sizes x 2 main photon energy ranges (below and above 1.5 keV) x 2 radiation source configurations = 48) makes it unrealistic to plan for a corresponding set of interchangeable reflecting surfaces.

The solution of choice, described hereafter, is therefore based on a set-up involving a reduced number of interchangeable mirrors. This solution presents two main characteristics requiring significant R&D development and determining a non-negligible risk factor. This is considered an acceptable compromise, considering that:

(i) a standard solution meeting all the above-mentioned requirements does not exist;

(ii) for each of the risk factors, the "backup solution" will still provide good enough performances;

(iii) all other characteristics can be attained with nearly standard solutions, finally reducing the total risk factor by a significant amount.

3.2.1   KB mirror system design

The KB system is designed according to the following details: for both vertical and horizontal focusing, two stripes with fixed-profile ellipses are shaped onto the same substrate, one beside the other, directly focusing the SASE3 undulator source in the two main interaction points F1 (AQS) and F2 (NQS) (Figure 3.2.1); for both the vertical (VFM) and horizontal focusing mirror (HFM) as well as both focusing conditions, the mirrors are 600 mm long (clear aperture) and the incidence angle is 13 mrad; the parameters defining the profiles and the surfaces are listed in Table 3.2.1.
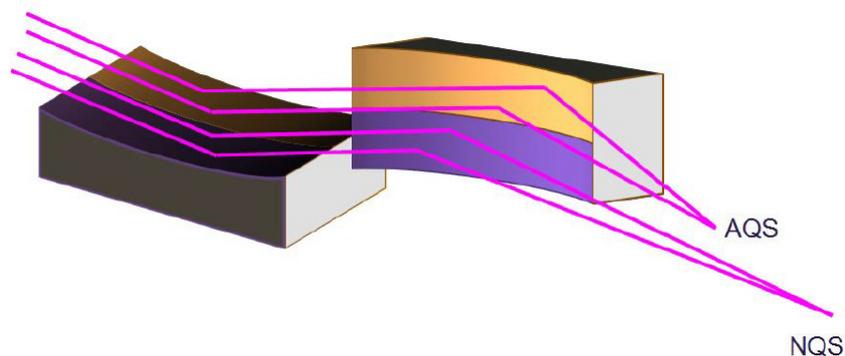
Figure 3.2.1: *Schematic representation of the KB mirror system design. For both vertical and horizontal focusing, two stripes with fixed-profile ellipses are shaped onto the same substrate, one beside the other, directly focusing the SASE3 undulator source in the two main interaction points F1 (AQS) and F2 (NQS).*

Table 3.2.1: Parameters describing the profile of the two KB mirrors focusing the FEL beam in the AQS (F1) and NQS (F2) interaction regions

Property	Unit	HFM F1	VFM F1	HFM F2	VFM F2
Clear aperture	mm x mm	600 x 25	600 x 25	600 x 25	600 x 25
p	m	443.0	442.3	443.0	442.3
q	m	2.0	2.7	4.188	4.888
Demagnification		221.5	163.8	105.8	90.5
Theta	mrad	13	13	13	13
Mean radius	m	306.32	412.88	638.29	743.80
Surface coating		bilayer	bilayer	bilayer	bilayer
Top layer, thickness	material, nm	B_4C,12	B_4C, 12	B_4C, 12	B_4C, 12
Bottom layer, thickness	material, nm	Cr, 120	Cr, 120	Cr, 120	Cr, 120
Slope error	nrad	50	50	50	50

The longitudinal profiles of the mirrors are shown in Figure 3.2.2. This configuration requires that the optical element labelled M_3 in Figure 2.6 (Chapter 2) is retracted from its working position so that the elements G_1, G_2, M_4, M_5 are bypassed by the FEL beam. The mirror pairs need moreover a carefully designed cooling system because of the high thermal load coming from the incident FEL radiation.

With this KB system design, all the requirements listed below are fulfilled:

■ **High transmission** of the KB mirror system. This feature is discussed in Section 3.2.2 together with the overall transmission of the beamline.

■ **Micro-focusing performances in the main interaction regions** F1 and F2 are obtained by the optimized mirror profiles and discussed in Section 3.2.3.

■ **Optimal focusing conditions in the F1' interaction region** are obtained by shifting the KB mirror system 390 mm downwards along the beam direction. The change in the value of source distance *p* (from [HFM, VFM] = [443.0, 443.3] to [HFM, VFM] = [443.39, 442.69]) is negligible and does

not significantly affect the mirror performances. The change in mirror position along the axis also changes the horizontal and vertical position of F1' by ~10.4 mm with respect to F1.

- **Focus size tuning** is obtained in all three interaction regions by incidence angle micro-detuning. The performances of the mirrors with respect to this feature are discussed in Section 3.2.4.

- **Monochromatic beam operation** is obtained in all three interaction regions by incidence angle detuning after insertion of the mirror labelled M3 in the beam path. The performances of the mirrors with respect to this feature are discussed in Section 3.2.5.
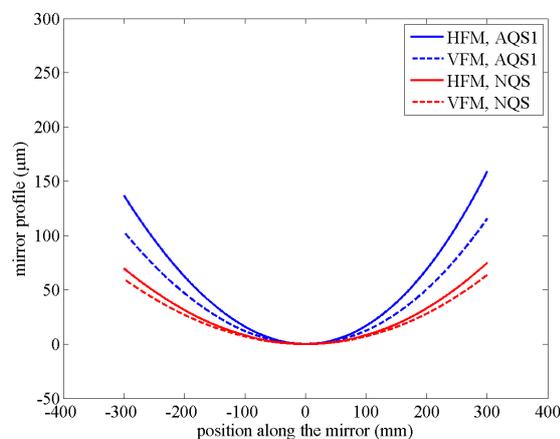
Figure 3.2.2: Profiles of the mirror surfaces calculated according to the ellipse equation and the parameters listed in Table 3.2.1. For the horizontal (vertical) focusing, the sag changes by ~ 60 (40) μm from AQS to NQS, making the solution based on a piezo-driven bendable mirror extremely challenging.

The following considerations have been taken into account for defining the mirror parameters:

- **Incidence angle**: An incidence angle as small as possible is desirable to get a lower curvature of the mirror surface (making the profile easier to manufacture) and higher surface reflectivity over a broader photon energy range. On the other hand, a larger incidence angle is desirable to increase the aperture of the mirror (resulting from the product of the mirror length and the incidence angle). The value of choice (13 mrad) represents the best compromise taking into account the selected mirror length and solution for the surface coating.

- **Macro-geometry**: The length of the mirrors determines the design of the moving system and the pointing stability affected by vibrations.
  The length of choice is slightly higher than that of the KB pair operating at the Coherent X-Ray Imaging (CXI) instrument at the Linac Coherent Light Source (LCLS), from which the concept for a feasible movement device can be inherited. With some development for vibration damping, the system pointing stability should be kept in the same range as for the surface error specified below for this mirror length.

  The HFM is the second mirror seen by the beam coming from the source. Its centre (downstream edge) is set to a distance of 770 mm (470 mm) from the exit flange of the KB mirror chamber thereby allowing for the 390 mm translation needed to focus the beam in the F1' interaction region using the same system. The length of the mirrors is close to the limit set by the maximum attainable value for the profile sag (edge-to-valley), which increases roughly quadratic with mirror length (see Figure 3.2.2).

  While drafting this document, the possibility of including a piezo-driven bending system for the mirrors has been considered. Within this solution, the focusing in the F1' interaction region would be obtained by changing the HFM-F1 and VFM-F1 curvatures of the mirrors to two profiles that we might call HFM-F1' and VFM-F1'. The difference in sag is yet quite high (15–20 µm) compared to the 300 mm available arm, making the technical realization of this feature an additional challenge. This solution is therefore not further considered here, though it would allow us to keep the focal distance smaller, because no movement of the mirrors is needed, and would not cause a different pointing for F1 and F1'.

  The VFM is the upstream mirror, as its horizontal (lying) position allows for equipping it with a more robust and effective cooling system, distributing the heat load from the source in a more rational way.

- **Mirror surface – coating**: A bilayer coating is identified as the only solution allowing a reasonable compromise for the incidence angle according to the criteria described above. The top layer is made of boron carbide (B_4C), selected because of its high and smooth reflectivity over a wide range above the C-K edge as well as its hardness and high thermal

capacity. The reflectivity drops above a threshold photon energy, which decreases with increasing incidence angle. This threshold is roughly 2.2 (3.0) keV for 13 (9) mrad. The bottom layer is made of Cr, with high reflectivity up to photon energies far above the SASE3 upper limit. Within the bilayer design, the high loading radiation in the low-photon energy range is being reflected by the B_4C layer and should not affect the Cr layer. Anyway, Cr is a transition metal with relatively low electron density, chosen to minimize the effect of hot electrons on the substrate surface. The B_4C layer is transparent to photon energies above 2.1 keV, which are then reflected by the Cr layer beneath. The reflectivity of a B_4C/Cr bilayer was calculated[1] varying both the top- and the bottom-layer thickness values, looking for the combination providing highest reflectivity performances.

The realization of a Cr/B4C bilayer coating is one major R&D challenge of the project. To our knowledge, a bilayer system involving B4C has never been developed and never been used in combination with an X-ray FEL source.

■ **Mirror surface – slope error**: The contribution to the spot size caused by the slope error can be estimated, if a reliable number for the slope error RMS is given: $d = 4 \times \sigma \times D$, where d is the contribution to the spot size (diameter FWHM), σ is the slope error RMS and D is the linear distance between the mirror and the focal point. At a distance of 2 (2.7) m, a slope error of 100 nrad causes a contribution of 0.8 (1.1) µm to the spot size. Aiming at a spot size substantially smaller than 1 µm in the AQS chamber restricts the requirement for the slope error to values below 50 nrad RMS. There is a single reference record [Siewert et al., Optics Express 20, 4525 (2012)] showing that this value can be attained by the use of deterministic polishing techniques. The realization of a mirror surface with such error specifications is therefore another R&D challenge.

The effective feasibility of the bilayer coating and its robustness against radiation damage are critical issues deserving further theoretical (Monte Carlo

---

[1] http://henke.lbl.gov/optical_constants/bilayer.html

simulations) and possibly experimental investigations. An alternative KB system design, not shown here, is based on two 800 mm long, 9 mrad incidence angle, B_4C-coated double-stripe mirrors. The performances of this system in terms of transmission would be very similar to the one of the bilayer solution, due to the combined effect of higher reflectivity, larger mirror length, and lower incidence angle. The micro-focusing performances are also comparable. Due to the larger mirror length, however, a strong R&D and budget effort has to be foreseen for developing the holding and movement system and for the polishing procedure.

The attainability of the surface error specifications is also, as already stated, a major challenge for the project. It is worth emphasizing that the B_4C/Cr bilayer solution is an ease factor for this feature, as it allows keeping the length of the mirror shorter compared to the B_4C single layer solution.

In case the bilayer solution is not viable, the possibility of coating two stripes (B_4C and Cr), one beside the other, for each curvature will be considered, at the expense of an overall larger mirror surface.

A radically different alternative to the solution proposed above consists in a mechanically actuated bendable KB system. This solution has not been considered in detail while drafting this document, because of the big technical challenges related to the use at the SASE3 beamline of the European XFEL. We are presently investigating the feasibility of such a system through various vendors.

3.2.2 Beamline transmission

At a given photon energy, the transmission of the beamline depends on the reflectivity of all optical elements and on the geometric transmission of the components with the smallest aperture with respect to the beam footprint. In the present optical layout, the mirrors involved are M_1, M_2 (offset mirrors), M_6, and M_7 (see Figure 2.6).

M_1 and M_2 are B_4C-coated, 6–20 mrad grazing incidence, 800 mm long. Their aperture relative to the footprint of the mirror is larger than the relative aperture of the KB mirrors. The total transmission can therefore be calculated as

(3.1) $t = r_1 \cdot r_2 \cdot r_7 \cdot r_8 \cdot f_7 \cdot f_8$

Where r_1 and r_2 are the reflectivity of B$_4$C at 9 mrad incidence, r_7 and r_8 are the reflectivity of the B$_4$C/Cr bilayer at 13 mrad incidence, f_7 and f_8 are the geometric transmission of the KB mirrors according to the value for the beam divergence given by Equation (3.1) of Chapter 5 of the CDR_BT [XFEL.EU TR-2011-02 (2011)], assuming the upper (worst-case) limit for the divergence to be valid.

Figure 3.2.3 shows the total transmission of the beamline as well as the individual contributions discussed here. Figure 3.2.4 shows the reflectivity of the B$_4$C single layer and the B$_4$C/Cr bilayer in the photon energy region of the C-K and Cr-L edges. The transmission function is fairly smooth over the central part of the photon energy range, limited in the low-energy range by the beam divergence and in the high-photon-energy range by the reduced transmission of the B$_4$C/Cr bilayer. The C-K and Cr-L absorption edges locally slightly affect (~ 3–7%) the transmission function.
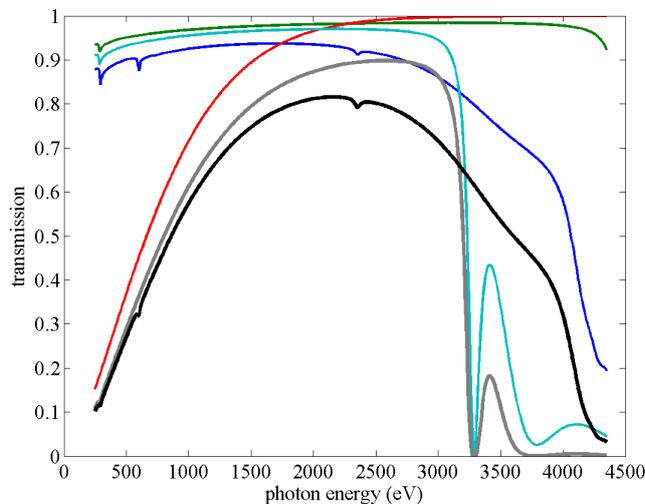
Figure 3.2.3: *Total transmission of the SASE3 beamline and the contributions of the individual components as a function of photon energy.* Blue: *Reflectivity of B$_4$C/Cr bilayer on a Si substrate. B$_4$C thickness is 12 nm, Cr thickness is 120 nm. Surface roughness is set to 1 nm for both layers and the substrate.* Green: *Reflectivity of B$_4$C single layer (50 nm thickness, 1 nm roughness). The reflectivity values are*

calculated[2] by setting the density values for B_4C and Cr to 80% and 90% of the bulk value, respectively. Red: f_7*f_8, *geometric transmission of the KB mirrors. The transmission is calculated from the integral of a Gaussian curve, the sigma given by the ratio of the beam footprint and the mirror aperture.* Black: *Total reflectivity, as defined in Equation (3.1).*
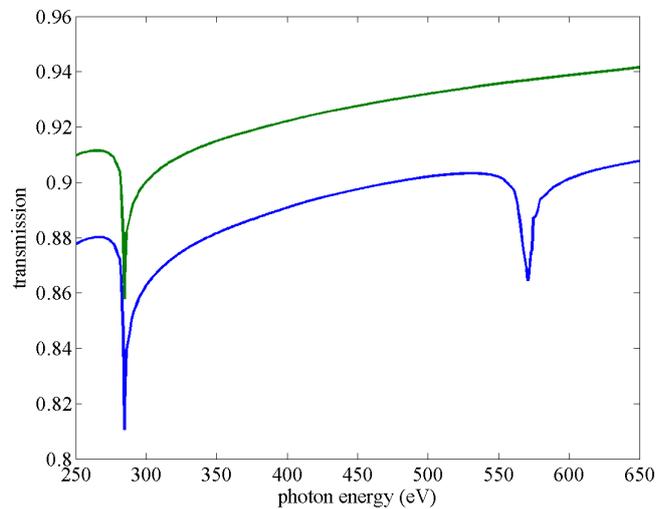
Figure 3.2.4: *B_4C/Cr bilayer (blue) and B_4C single-layer (green) reflectivity in the C-1s and Cr-2p edge regions, calculated as in Figure 3.2.3*

The set value for the incidence angle in a curved mirror corresponds to the value at the pole position. The local incidence angle varies along the mirror profile and possibly affects the reflectivity and transmission properties. In the case of the KB mirror system under discussion, this is not a critical issue as the incidence angle varies only by a small amount (Figure 3.2.5) and the reflectivity of B_4C/Cr varies smoothly in this range. Yet, as in the high-energy range the reflectivity increases slightly with decreasing incidence angle, the lower incidence angle seen by the beam on the left (upstream) part of the mirror can be exploited if experiments at high (> 3 keV) photon energies are to be performed, because the divergence is much smaller and therefore the small beam spot hits only one part of the mirror. By moving the mirror in the transversal plane, it is possible to match the footprint with the locally lower

---

[2] http://henke.lbl.gov/optical_constants/bilayer.html

incidence angle, getting better transmission performances for the high-photon-energy beam.
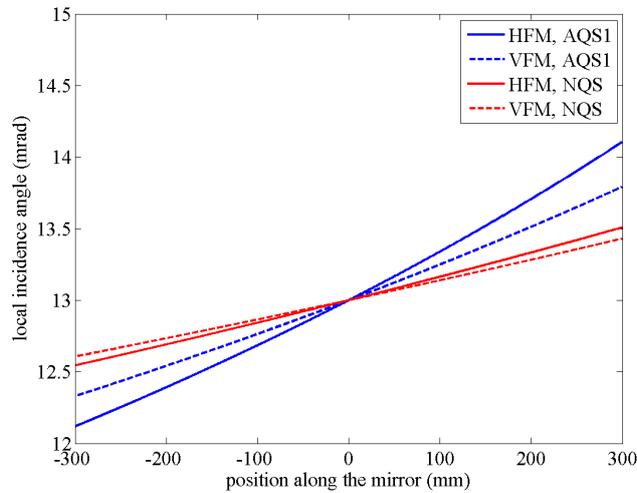
Figure 3.2.5: *Local incidence angle along the mirror profile (see text)*

3.2.3   KB mirror system micro-focusing performances

Figures 3.2.6 and 3.2.7 show the spot size and the depth of focus in the F1 / F1' (AQS) and the F2 (NQS) interaction points.

The spot size is calculated including geometric demagnification of the source (assuming no aberration effects), diffraction effects from the finite size of the mirrors, and slope error effects. The latter effects are calculated as $4 \times D \times \sigma$, where D is the image distance from the focus and σ is the slope error RMS. The slope error is the main source of spot size degradation at high photon energies, as can be seen from the comparison with the ideal surface calculation.

The depth of focus, defined as the length of the region along the beam axis where the beam intensity is more than half the maximum, is always in the few-millimetre range. Alignment with the sample along the beam axis is therefore not expected to be a critical issue.
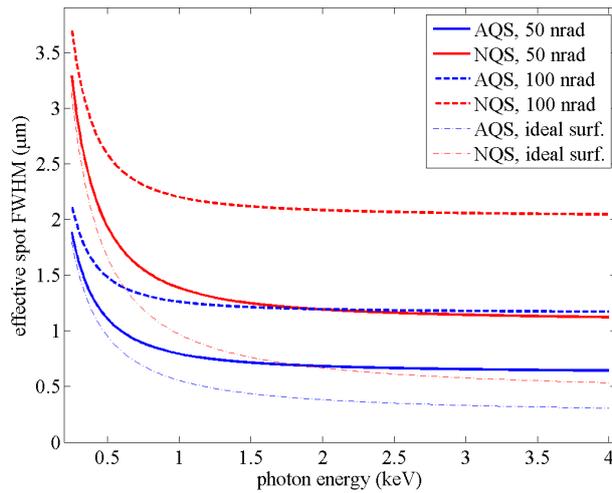
Figure 3.2.6: *Expected spot size in the main interaction region of AQS (F1) and NQS (F2) assuming a 50 nrad and a 100 nrad RMS slope error. Effective spot FWHM is calculated as sqrt (FWHM$_{vert}$ x FWHM$_{horiz}$). The spot size calculation includes geometric optics, diffraction effects, and slope error effects. As a reference, the spot size produced by an ideal surface (neglecting slope error effects) is represented.*
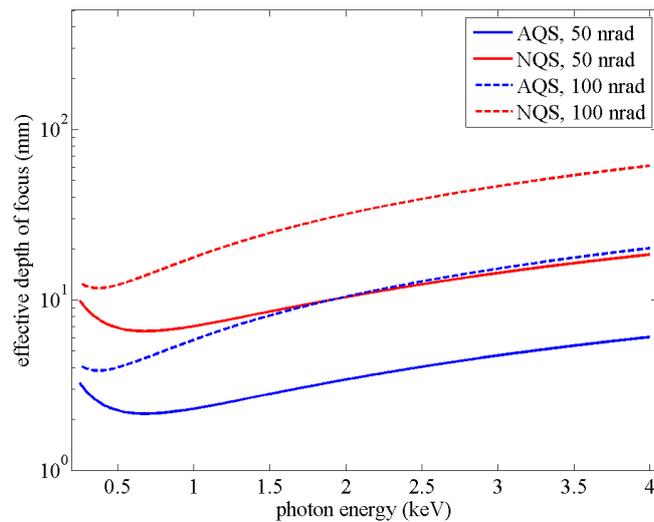
Figure 3.2.7: *Expected depth of focus in the main interaction region of AQS (F1) and NQS (F2) assuming a 50 nrad and a 100 nrad RMS slope error. The depth of focus along the beam axis is defined here as twice the distance between the focal point and the point where the intensity is half of the value in the focus.*

3.2.4   Tuning spot size by KB mirrors incidence angle detuning

The size of the X-ray spot in the interaction region can be increased continuously up to several tens of µm by detuning the incidence angle of the KB mirrors in the range of some tens of µrad. The detuning required to attain a given spot size can be calculated on a first approximation based on geometric optics (Figure 3.2.8) and then directly tested by ray-tracing simulations.
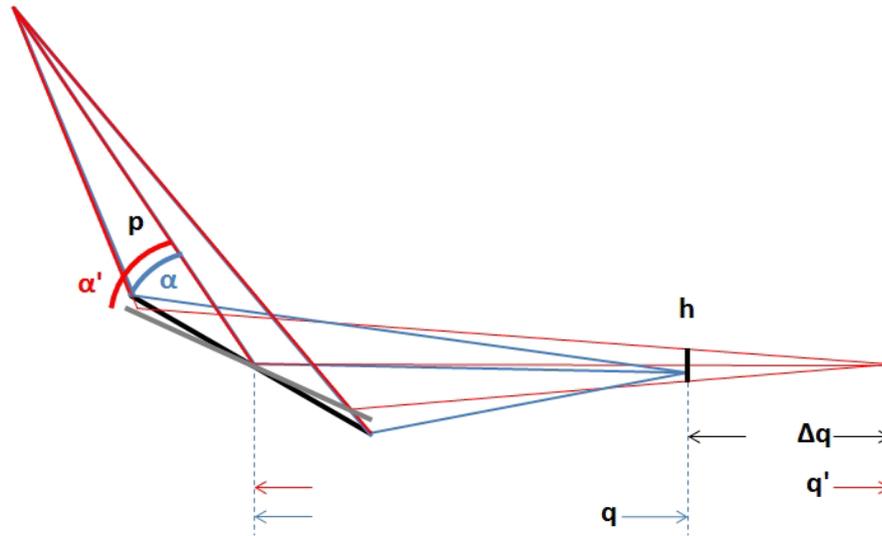
Figure 3.2.8: Schematic representation of the spot size detuning by detuning of the incidence angle. The image distance changes with the incidence angle according to Equation (3.3). If the change in the image distance is small, the beam section in the original image position h is just the projection of the footprint on the mirror f, and its size is proportional to the image displacement dq/q (Equation 3.4).

The average radius of curvature for each of the mirrors listed in Table 3.2.1 is calculated from source distance p, image distance q and incidence angle α according to

$$(3.2) \quad R = \frac{2}{\sin \alpha} \cdot \left(\frac{1}{p} + \frac{1}{q} \right)^{-1}.$$

For a given radius of curvature R, the image distance can be changed to a value q', if the incidence angle is detuned to a value α' given by

$$(3.3) \quad \alpha' = \sin^{-1} \left(\frac{2}{R} \cdot \left(\frac{1}{p} + \frac{1}{q'} \right)^{-1} \right).$$

If the displacement of the image point dq = q' – q is small, the spot size in position q can be linearly approximated as

$$(3.4) \quad h = \frac{dq}{q} \cdot f$$

where f is the FWHM size of the beam on the mirror, which is determined by the photon-energy-dependent source, and h is the FWHM size of the spot in the original image position q (Figure 3.2.8).

Substituting q' = q + dq from Equation (3.4) into Equation (3.3), one gets the value of the incidence angle that is producing a spot size of h in the original image position q. The [α',q] relationship is energy-dependent due to the energy-dependent size of the footprint on the mirror. Calculated values for $\alpha'-\alpha$ for different photon energies and spot size are shown in Figure 3.2.9 for the AQS VFM mirror.
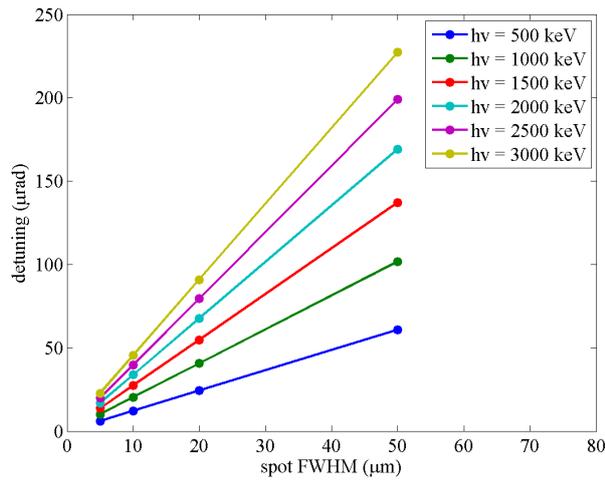
Figure 3.2.9: $\alpha'-\alpha$ *dependence on the spot size h in the F1 interaction point for different photon energies. The detuning values are calculated for the vertical mirror VFM. According to Equations (3.2) and (3.3), the detuning of HFM has to be ~ 0.4% lower.*

X-ray tracing simulations have been performed using the Shadow extension of the XOP2.3 package for selected detuning angles and photon energies. Detuning angles are set to the photon-energy-dependent values relative to the selected spot size (Figure 3.2.9). Simulations are performed for the F1

interaction point. Ideal surfaces are assumed for the simulation. A subsample of the results is shown in Figure 3.2.10.
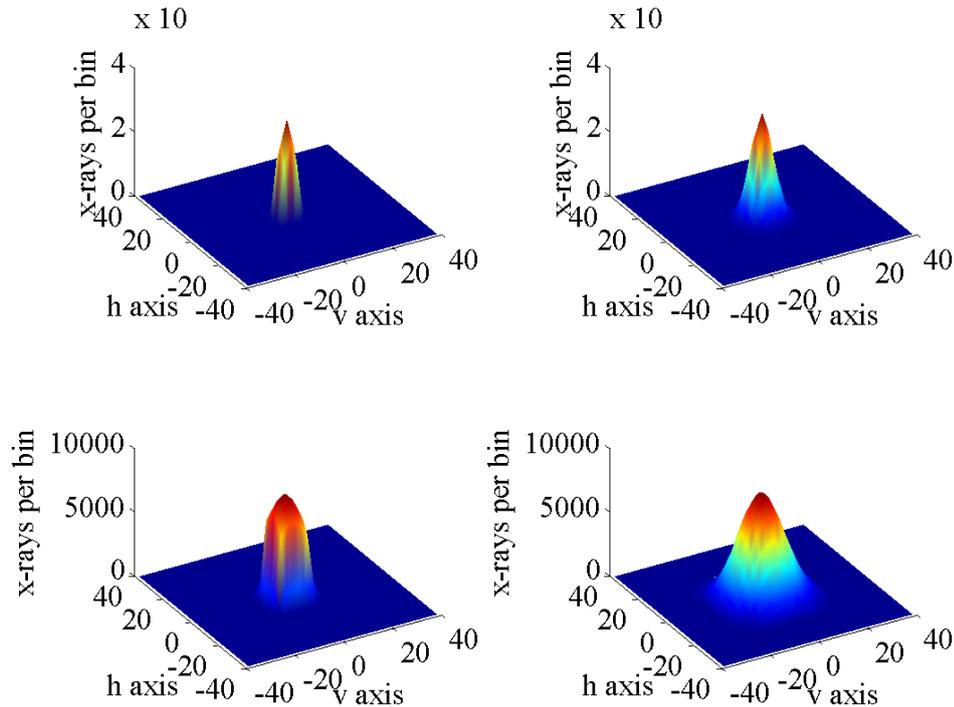
Figure 3.2.10: 2D representation of the intensity profile in the AQS interaction point (F1) for different photon energies and detuning angles. Top left: hν = 0.5 keV, detuning set to 10 µm spot size. Top right: hν = 2.5 keV, detuning set to 10 µm spot size: Bottom left: hν = 0.5 keV, detuning set to 20 µm spot size. Bottom right: hν = 2.0 keV, detuning set to 20 µm spot size. At low photon energies, the effect of the finite size of the mirror is quite evident in the spot shape.

The ray tracing shows that the spot size in the original interaction point is substantially the projected image of the footprint on the mirror. The detuning angle and the image displacement are on the order of 1–2%, low enough to keep the spot shape substantially unaffected. For low photon energies, the shape is affected by the finite size of the mirrors, and this results in a cut-off along both vertical and horizontal directions for the beam profile in the interaction region.

The FWHM of the simulated profile corresponds within fair agreement to the value set obtained when defining the detuning angle by Equation 3.3 (Figure 3.2.11).
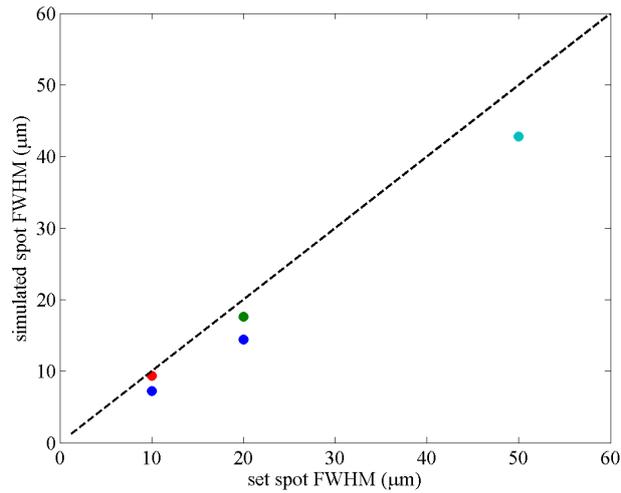
Figure 3.2.11: *Comparison between set spot FWHM and the FHWM as extracted from the simulated spot intensity profile (horizontal axis). Simulations are performed at different photon energies (blue = 0.5 keV; green = 2 keV; red = 2.5 keV; cyan = 3 keV), tuning the incidence angle to the values relative to the spot size set point. Two independent factors, namely the approximation expressed in Equation 3.4 and the finite size of the mirror, cause the slightly smaller spot size with respect to the set value.*

Detuning the incidence angle causes a non-negligible displacement of the spot position in the interaction point plane. The amount of this displacement is estimated for F1 from the mean position of the simulated rays in the interaction point. Vertical and horizontal displacements are shown in Figure 3.2.12 as a function of detuning angle.
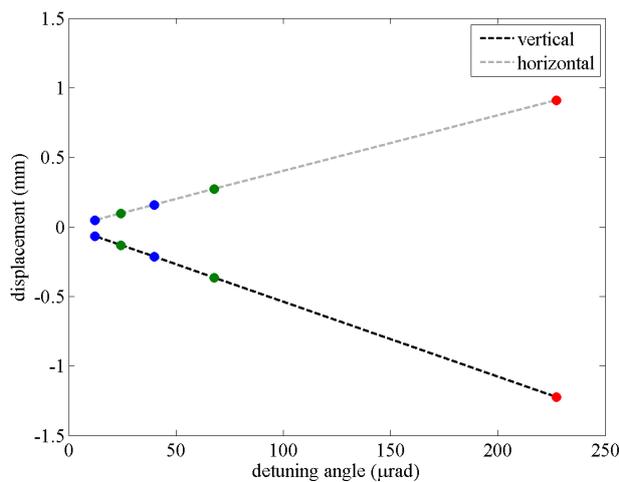
Figure 3.2.12: *Horizontal and vertical displacements of the focal spot in the transverse plane are shown as a function of incidence angle detuning.*

3.2.5 Changing operation mode from pink to monochromatic beam

The source point of the monochromatic beam is the exit slit of the monochromator, i.e. the focal point of the vertical intermediate focusing (IMF) mirror M_3. This is about 48 m upstream the KB, while the undulator, which is the source point for the pink beam, is ~ 445 m before the KB. Detuning of the incidence angle can be used here to focus the monochromatic light in the AQS and NQS interaction regions using the fixed-radii mirrors defined in Table 3.2.1. In analogy to the detuning procedure for increasing the spot size, the proper incidence angle

$$(3.5) \quad \alpha' = \sin^{-1}\left(\frac{2}{R} \cdot \left(\frac{1}{p'} + \frac{1}{q}\right)^{-1}\right)$$

can be defined for each of the KB vertical mirror positions, with R and q from Table 3.2.1, and p set equal to 48 m. As there is no intermediate focusing on the horizontal plane, the HFM does not need to be detuned.

The value of α' is 12.38 mrad for AQS and 11.93 mrad for NQS. The shape of the focal spot in this intermediate detuning regime (4–8% detuning) for the incidence angle is slightly affected by aberration and depends on divergence, i.e. photon energy, as demonstrated by the ray-tracing simulations (Figures 3.2.13 and 3.2.14).
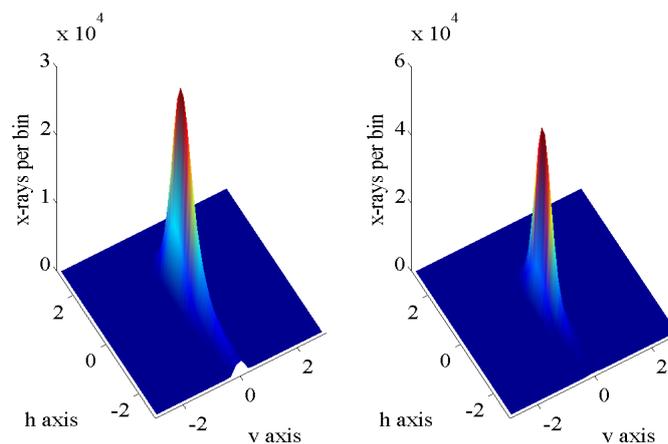
Figure 3.2.13: 2D image of the AQS focal spot at 1 keV (left) and 2.5 keV (right) incident photon energy. The beam is optimally focused along the vertical plane, whereas the focusing in the horizontal plane shows slight divergence-dependent aberration.
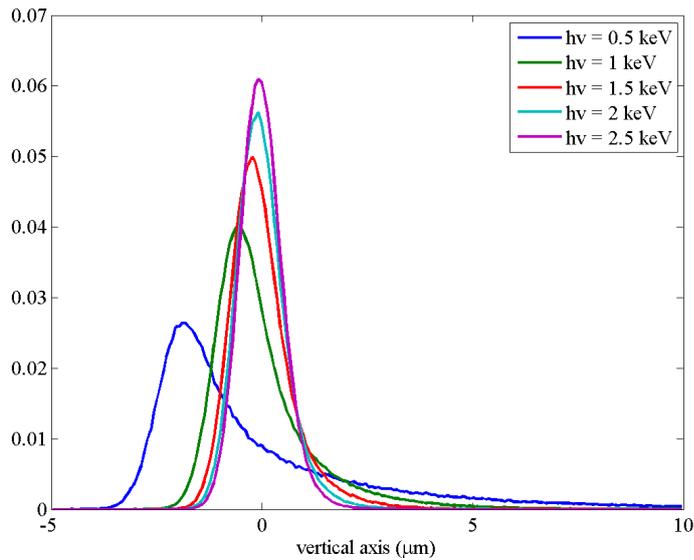
Figure 3.2.14: Vertical profiles of the monochromatic beam in the AQS focus for different photon energies. The profiles are normalized to the transmission of the optics.

As discussed already for the spot size tuning, detuning the incidence angle causes a non-negligible displacement of the spot position in the interaction point plane. The amount of this displacement is 3.5 (6.1) mm in the vertical plane for the AQS (NQS) interaction point.

3.3   SQS experiment station

3.3.1   AQS chamber

In order to ensure a high versatility in experimental techniques for gas phase experiments and to host the corresponding number of spectrometers for electron, ion, and photon analysis, the AQS chamber is subdivided into two sectors with almost equal focus conditions. The two interaction regions centred around the focus positions F1 and F1' are separated by 39 cm, which is the shortest possible distance with respect to geometrical and practical constraints. Since the beam size at F1' is about 1.5 mm, when the main focus is set to the F1 position, the spectrometers in section F1' can be used also for online FEL beam characterization with respect to wavelength and intensity.

A schematic view of the AQS chamber and its individual components is given in Figure 3.3.1, the mechanical design is shown in Figures 3.3.2a, b, c.
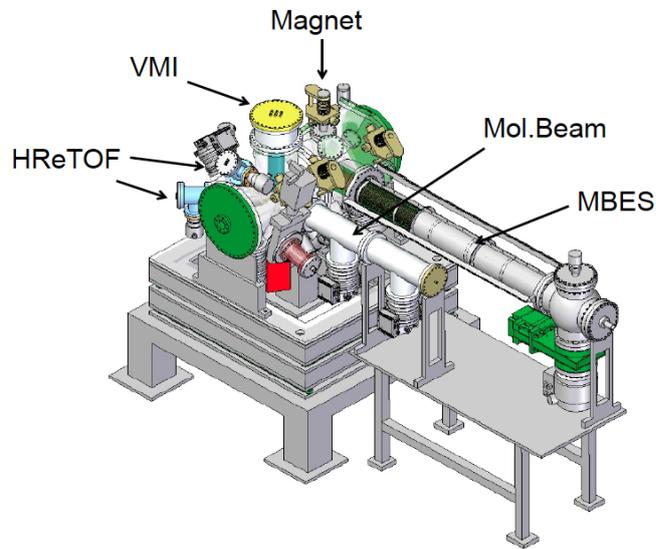
Figure 3.3.1: *Schematic view of the AQS experiment chamber*
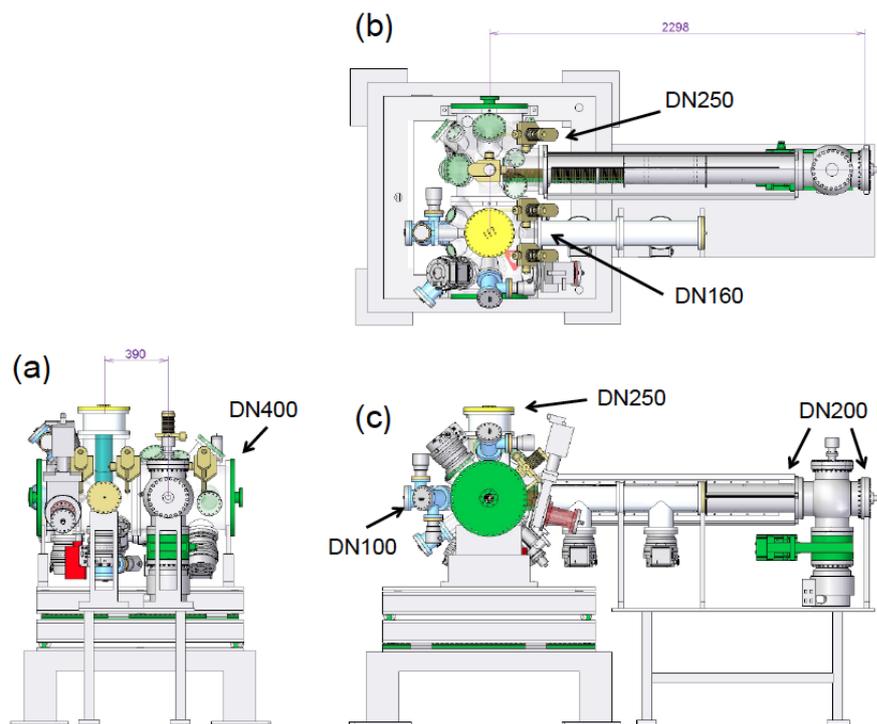
Figure 3.3.2: *AQS experiment chamber: (a) side view, (b) top view and (c) front view. Some of the principal distances and port size parameters are indicated. For convenience the tilt of the experiment chamber imposed by the KB optics is not represented.*

The alignment of the AQS chamber with respect to the FEL beam is realized with a set-up enabling translation (50 mm) and rotational movements of the vacuum chamber with a precision of less than 0.5 μm.

The first interaction zone, at focus position F1 (Figure 3.3.3), is surrounded by 1 molecular beam apparatus, up to 6 (minimum 5) high-resolution time-of-flight spectrometers (HReTOF) and 1 velocity-map-imaging (VMI) spectrometer (see Table 3.3.1). The optimized geometry of the entrance optics as well as adapted alignment procedures for the spectrometers ensure the unperturbed access to the interaction zone for the FEL beam, the optical laser, and the diagnostic paddle.

Table 3.3.1: *Spectrometers used in the AQS experiment chamber*

Analyser	Focus	Acceptance	Resolution	Notes
HReTOF	F1	< 0.5% of 4π	$E\,/\,\Delta E > 10^4$	Angle-resolved, non-dipole, e-e coincidence spectroscopy
MBES	F1'	> 50% of 4π	$E\,/\,\Delta E \approx 10^2$	Single-shot capability
VMI	F1	4π	$E\,/\,\Delta E \approx 10^2$	Full angular distribution, e-ion coincidences
XUV spectrometer	F1'	< 1% of 4π	$E\,/\,\Delta E > 10^4$	Insensitive to space charge
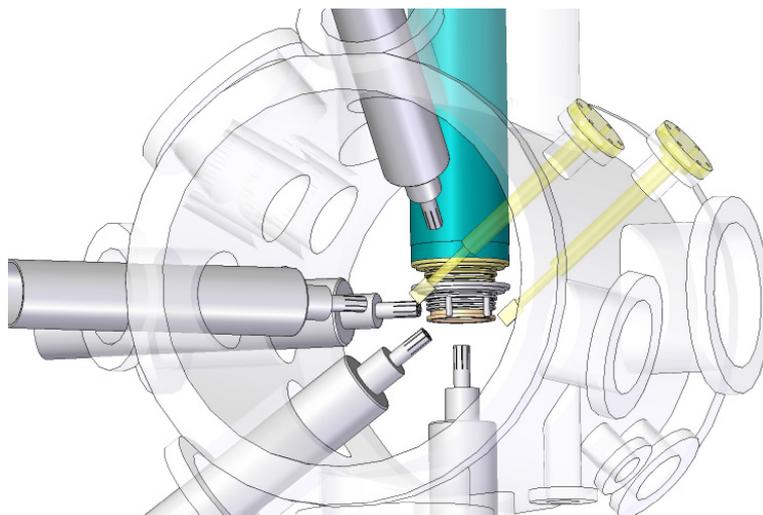
Figure 3.3.3: *Zoom into the interaction region around F1*

3.3.1.1 HReTOF spectrometer

A set of five high-resolution electron time-of-flight spectrometers (HReTOF) is used for measurements requiring a high kinetic-energy resolution and/or the determination of the angular distribution of the electron emission.

The design of these TOF spectrometers is determined by the aim to ensure, for a large number of experiments, a kinetic-energy resolution $E/\Delta E \geq$ 10 000. The final layout will be close to that given by Hemmers et al. [Rev.Sci.Instrum. 69, 3809 (2010)] (Figure 3.3.4), but with the limitations that some characteristics, i.e. total length and precise geometry of the entrance and retardation optics, have to be modified and adapted to the SQS applications on the basis of electron ray-tracing simulations, using e.g. the SIMION program.

As a first step, a compilation of parameters for similar spectrometers has been undertaken comparing eTOF spectrometers, which are already in use at:

(A) the AMO end station at LCLS [Hemmers et al., Rev.Sci.Instrum. 69, 3809 (2010)],

(B) the P04 end station at PETRA III [Viefhaus et al., in preparation (2012)],

(C) FLASH and LCLS [www.kaesdorf.de]

(D) BESSY etc. [ArtOf 10k, www.vgsscienta.com].

Table 3.3.2: Comparison of the performances of different TOF spectrometers

Parameter	(A)	(B)	(C)	(D)
Energy range	Wide energy range incl. hard X-rays	Wide energy range incl. hard X-rays	Soft X-ray limitation (< 1keV)	Soft X-ray limitation (< 1keV))
Single-shot capability	Partly	Yes	Yes	Reduced
Max. energy resolution	10^3 to (theoretically) 10^4	$>10^3$	$>10^2$	10^3 to theoretically $>10^4$
Retardation / resolution recovery	Up to 1 keV	Up to 3 keV	Up to 0.18 keV	Energy window selection $\rightarrow$ max 1 keV
Flight tube length (m)	0.4375	0.14	0.35	1.0
Working distance (mm)	Variable	Variable	3 mm	39 mm
Acceptance angle (% of 4π)	0.056	0.2	3.8	1.75
ARPES application	Yes	Yes	No	Intrinsically yes
Angular resolution	High	Medium	Medium	High
Minimal E_{kin} for 4.5 MHz FEL rep. rate	13	1.2	7.1 (20)	Outside specification
Multi-channel plate (MCP) assembly	42 mm (active) detection quality chevron	25 mm (active) detection quality, z-stack	50 mm (total) detection quality chevron	40 mm delay line MCP assembly with spatial resolution
Misc.	compact	very compact	Large design – difficult multi-spectrometer use	Large design – no multi-spectrometer use

This comparison shows that the spectrometers (C) and (D) are mainly designed for the analysis of electrons with kinetic energies below 1 keV and are difficult to combine with other spectrometers (e.g. VMI) for performing coincidence measurements. Principal advantage is the relative large

acceptance angle, which enables measurements with high single-shot statistics. The spectrometer (A) and (B) provide the required energy resolution of >10^4, though at the expense of much lower acceptance. The redesign of spectrometer (A) focusing on its larger energy and angular resolution and taking into account the latest expertise obtained during design and commissioning of spectrometer (B) is foreseen for the HReTOF spectrometer at the AQS end station.

Simulations of the electron trajectories for the different geometries show that:

(i) within an inter-pulse period of the European XFEL (220 ns), electrons with kinetic energies larger than 13 eV can be recorded for the longest of the spectrometers (A) (Figure 3.3.4),

Electron Time-of-Flight for different TOF-designs
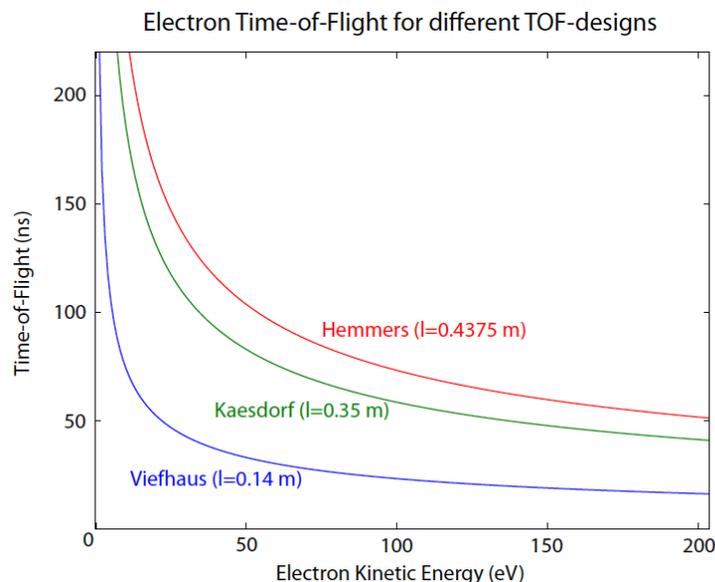
Figure 3.3.4: Time-of-flight for electrons with kinetic energies up to 200 eV calculated for the different TOF spectrometers considered here. The dashed line represents the time interval between two consecutive FEL pulses at 4.5 MHz repetition rate.

(ii) the relative energy resolution is in the order of a few per cent in the kinetic energy region below 1000 eV kinetic energy (Figure 3.3.5a), i.e. by applying an adequate retardation to the incoming electrons, an absolute resolution of 10^4 can be reached. For example, electrons with 1000 eV kinetic energy can be measured at 50 eV with a resolution of 0.2 %, i.e. 100 meV. This value will be achievable by minimizing the principal sources of flight time uncertainties

(Figure 3.3.5b), in particular by reducing the uncertainty in timing, which gives the main contribution to the overall resolution.
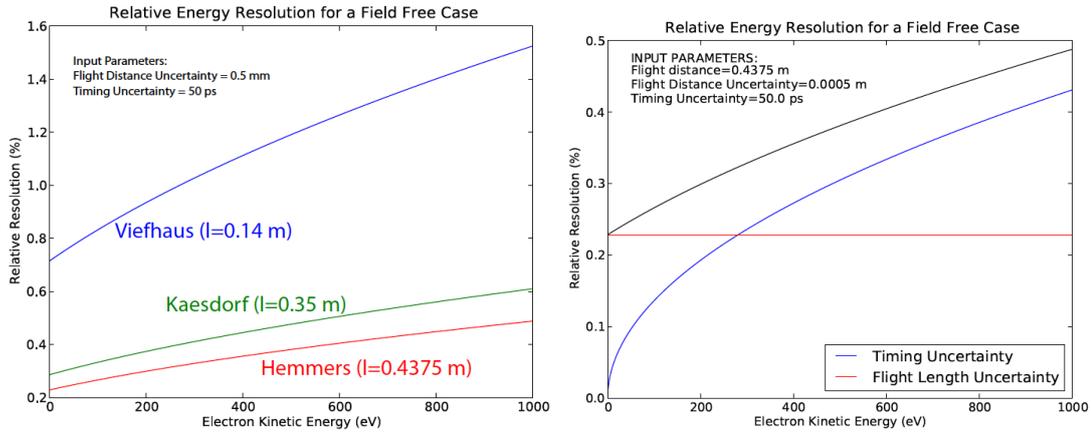
Figure 3.3.5: *(a) Relative energy resolution for different TOF spectrometers. (b) Decomposition of the energy resolution into the contribution from the flight length Δl and the timing uncertainties Δt.*

A typical layout of the spectrometer, which is closest to the required performances, is given in Figure 3.3.6. The technical parameters are listed in Table 3.3.3.
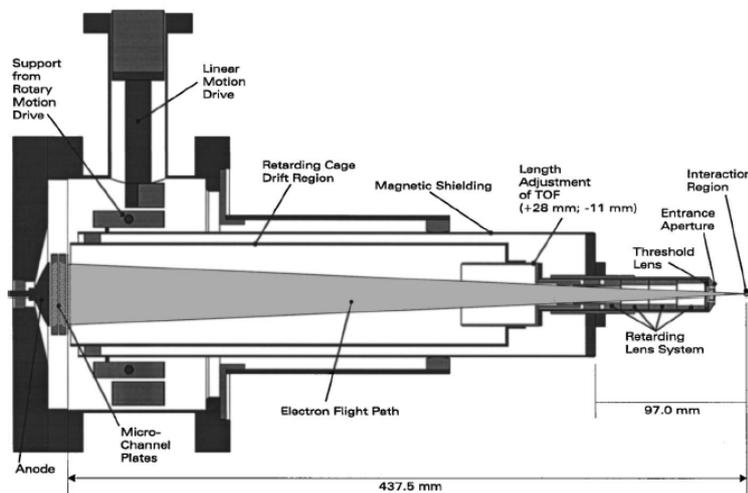
Figure 3.3.6: *Scheme of the HReTOF spectrometer [see Hemmers et al., 2010]*

Table 3.3.3: Principal characteristics of the HReTOF

Overall length:	47.2 cm
Length of TOF	43.8 cm
TOF diameter	10.0 cm
Lens diameter	2.2 cm
Distance to interaction volume	2 cm
Detector type	MCP
Detector size	42 mm

All HReTOFs are shielded against external magnetic fields by a mu-metal tube. They are equipped with a set of multi-channel plate (MCP) detectors and fast readout electronics. The detector region is pumped separately by a small turbo pump in order to ensure optimal functioning of the MCPs. For the optimization of the overlap between the acceptance cone of the spectrometers and the interaction zone, the distance to the FEL beam and two tilt angles can be adjusted independently for each of the HReTOFs.

Three TOF spectrometers are mounted in the so-called dipole plane, i.e. perpendicular to the FEL beam propagation direction, at angles $\vartheta = 0°$, 54.7°, and 90° with respect to the linear (horizontal) polarization vector of the XUV radiation. The electron angular distribution for a one-photon and a two-photon ionization processes, characterized by the asymmetry parameters β_2 and β_4 [A. Grum-Grzhimailo, internal report], can be determined using this configuration. The spectrometer mounted at 54.7° enables measurements of the relative cross sections, i.e. electron spectra independent of the angular distribution.

In addition, non-dipole effects can be studied when using two (eventually three) additional spectrometers. They are mounted out of the dipole plane at angles:

TOF 4: $\vartheta = 0°$, $\varphi = 45°$

TOF 5: $\vartheta = 90°$, $\varphi = 45°$

The additional implementation of the sixth spectrometer at:

TOF 6: $\vartheta = 30°$, $\varphi = 45°$

finally enables the determination of all parameters (β_2, β_4, δ_2, γ_2, γ_4), which are describing the non-dipole phenomenon [A. Grum-Grzhimailo, internal report]:

$$\frac{d\sigma_2}{d\Omega_2} = \frac{\sigma_2}{4\pi} \left(1 + \beta_2^{(2)} P_2(\cos\vartheta_2) + \beta_4^{(2)} P_4(\cos\vartheta_2) \right.$$
$$\left. + \; (\delta^{(2)} + \gamma_2^{(2)} \cos^2\vartheta_2 + \gamma_4^{(2)} \cos^4\vartheta_2) \sin\vartheta_2 \cos\varphi_2) \right)$$

where β_2, β_4 represent the asymmetry parameters for the two-photon ionization process and δ and γ are the non-dipole parameters. ϑ and φ are respectively the angle in the dipole plane and the angle between the photon propagation axis and the projection of the electron momentum into the vertical plane including the photon beam.

The vertically oriented HReTOF (TOF 3) can also be used for ion detection by inversion of the polarity of the used potentials. The acceleration of the ions towards the entrance of the TOF spectrometers is realized by applying an electric field around the interaction region using the VMI electrodes.

The HReTOF spectrometer will be equipped with an MCP detector, which is currently the best solution for charged particle detection: it encodes particle detection events in electric-current pulses to be acquired in an ADC framework, features high dynamic range and high timing resolution and, coupled to a phosphor screen or a delay line system, allows position-sensitive detection. The performances in terms of resolution and dynamic range can be characterized on the basis of the following features, including the structural parameters of the MCP and its interface to the analyser and to the DAQ system:

- The **pore size** determines the duration of the pulse and of its rising edge, which is roughly proportional to the attainable timing resolution, if no other factor is limiting it. The smaller the pore size, the shorter the pulse duration can be. At present, MCPs with pores as small as 2 μm can be

produced [http://bit.ly/M1m3So], giving a pulse duration <100 ps FWHM at the expense of a poor signal-to-noise (S/N) ratio, poor pulse shape quality, and MCP fragility.

- The **detector diameter** determines the acceptance angle and ultimately the detection efficiency; if high timing resolution (<100 ps) is envisaged, this parameter has to be taken into account, as it is determining the time dispersion due to finite signal travelling time across the detector surface. As a result, a timing resolution better than ~120 ps is not attainable with a detector diameter of 80 mm.

- The aspect ratio of the pores is normally set to an optimized value around 60. This value together with the pore diameter (size) determines the **thickness of the plate**, which in its turn gives an upper limit for the diameter. The thickness of the MCP also affects the S/N ratio and the overall quality of the signal shape, which together with the pulse duration is the main factor influencing the attainable timing resolution.

- In most of the cases, stacks of MCPs are used to get higher signal gain and dynamic range. The choice for a **z-stack of a chevron configuration** (3 or 2 plates in series) is also determining the trade-off between the attainable S/N ratio and pulse duration, both affecting the timing resolution.

- The **readout circuit and electronics** are a critical component of the detector, determining the overall quality of the signal shape, including its dependence on the intensity level, and the level of signal ringing. Both these aspects of the signal trace affect the reliability of any centre-of-mass (COM) reconstruction algorithm in the online analysis.

At present, a detector solution featuring a pulse width substantially smaller than 1 ns (i.e 600–700 ps) and at the same time a good quality for the pulse shape and for the S/N ratio is a reasonable objective to be pursued. A timing resolution of 50 ps (counting mode) can be envisaged by matching such a detector with an ADC system with a proper speed and dynamic range [J. Viefhaus, private communication].

For this purpose, some R&D effort, including testing of different MCP models, needs to be started in the coming months.

3.3.1.2 VMI spectrometer

The velocity-map-imaging spectrometer (VMI) is used for measurements of the angular distribution of photoelectrons or ionic dissociation fragments. The high collection efficiency also enables coincidence studies in combination with one of the HReTOF spectrometers.

The design will follow the concept developed for the VMI spectrometer used for high-kinetic-energy operation at LCLS [M. Vrakking et al., Max-Born-Institute, Berlin] aiming to measure the full angular distribution of photoelectrons with an energy resolution of about $E/\Delta E$ = 100. The VMI will be used for electron and ion analysis; the final design will be based on the latest developments and experience obtained at LCLS and at high-energy synchrotron radiation beamlines. A general scheme for a typical VMI spectrometer is given in Figure 3.3.7; the main characteristics are listed in Table 3.4.4. A detailed simulation will be performed in order to define the final layout. A magnetic shielding will be installed around the VMI.
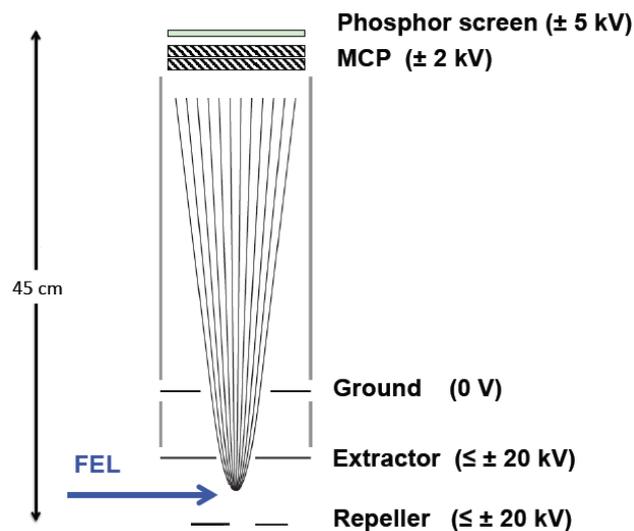
Figure 3.3.7: *Schematic view of the VMI spectrometer*

Table 3.3.4: Principal characteristics of the VMI

Overall length	40 cm
TOF diameter	80 mm
Distance to interaction volume	1 cm
Detector type	2D imaging MCP with delay line anode and phosphor screen
Detector size	80 mm

It is envisaged to equip the VMI with an MCP-based position-sensitive detector, which might consist, depending on the specific application, either of a delay line detector (DLD) with multi-hit capability or of a phosphor screen coupled to a megapixel CCD (PS-CCD). The DLD system is optimally fitting to the MHz repetition rate of the FEL source. It can detect multiple particle hits (multi-hits) and reconstruct the position and time coordinates ("3D-detection") for each individual particle (hit), thus enabling TOF–VMI ion–electron / electron–ion coincidence measurements. Even when operated in a coincidence measurement scheme, the detector is designed for collecting "few" (<10) particles per "production cycle" (FEL pulse) with a rate tolerance of 1 MHz or above depending on the model. Higher multi-hit capability can be attained by introducing a delay anode system with three independent delay line layers in a hexagonal geometry, according to the Roentdek design [www.roentdek.com/info/Delay_Line]. Such a system, together with a software constant-fraction discrimination method, allows the extraction of the full time–position information for each of up to several tens of charged particles produced in a time window of 100 ns [K. Motomura et al., NIMA 606 (2009) 770]. Position and time resolution of the detector depend to a large extend on the readout electronics [Vallerga et al., Proc. SPIE Vol. 4139, p. 34-42], which will be carefully designed. For measurements where no single-detection event timing capability is required, a PS-CCD system may be employed. This system, based on a CCD readout, does not allow MHz repetition rate measurements. On the other hand, the only limitation to the number of

particles that can be collected is given by the MCP/phosphor screen saturation threshold.

Around the F1' focus, the magnetic-bottle electron spectrometer (MBES) and the XUV fluorescence spectrometer will be installed (Figure 3.3.8). When using the XUV spectrometer, the strong magnet is removed in order to provide the space for the entrance aperture for the spectrometer.
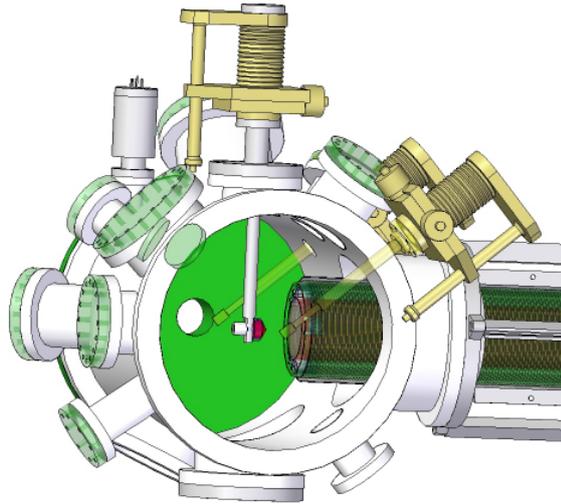
Figure 3.3.8: Zoom into the interaction region around F1'

3.3.1.3   High-resolution XUV fluorescence spectrometer

In many cases involving many-photon processes, a large number of ions and electrons are formed during the XUV pulses. The precise analysis of electrons and ions is therefore strongly affected in some cases (multiple ionization). Here, the photon scattering spectroscopy can provide similar or complementary information on the processes. Since the radiative decay is generally weak in the soft X-ray regime compared to the electronic relaxation, the XUV spectrometer will be used in combination with a specially designed gas cell allowing higher gas pressure to be used. The energy resolution of the spectrometer will be about 10 000, which is sufficient to resolve most of the vibrational structures of small molecules.

The proposed spectrometer is a Swedish in-kind contribution (J.E. Rubensson, J. Nordgren, University of Uppsala) and the technical specification is under study. The spectrometer will be used for non-linear soft

X-ray spectroscopy, but will also incorporate an entirely new feature, which is suitable for the exploitation of the extreme time structure of the European XFEL, namely an imaging capability that allows ultrafast timing X-ray emission and scattering experiments. One method to establish a timescale in an X-ray scattering experiment is to arrange for a grazing-incidence illumination of a sample so that the distance along the sample determines a time span. The temporal evolution of the excitation by a short laser pulse can then be revealed by studying the signal along the sample. Also, the study of non-linear phenomena occurring in the interaction of the high-intensity FEL beam with a medium would benefit from a possibility to monitor the emission signal at various positions along the beam. This can be accomplished by imaging the source (a short distance along the beam) in the plane perpendicular to the dispersion plane of the spectrometer by means of a mirror (Figure 3.3.9). This mirror is also used to increase the luminosity of the instrument, since the astigmatism of grazing-incidence optics tends to keep the acceptance angle small. In order for this to be feasible without varying the focal length of the imaging mirror, the optical distance between source and detector should be kept constant. One possibility to accomplish this could be to use a VLS grating for constant focal length. Another way, using Rowland geometry, would be to move the grating rather than the detector when changing the photon energy. When doing so, moving the grating towards the source leads to a more grazing angle of incidence. This would preferably be associated with moving towards higher photon energies, and this is the case for negative (inside) order of diffraction. An instrument optimized for negative order of diffraction could thus be designed to meet the requirements.

Figure 3.3.9 shows the optical layout of a 1D imaging XUV spectrometer based on negative-order diffraction. In this case, the grating is moved in an X-Y-Φ coordinate system with high accuracy in order to cover the energy range in question. The cylindrical imaging mirror requires a constant focal length. The imaging mirror images the source onto the detector in the sagittal plane (plane of paper) and the grating disperses the spectrum in the perpendicular plane. The recorded spectrum will represent the X-ray emission from different parts of the source as a 2D image, the dispersion appearing in one direction and the elongation of the source in the other. Figure 3.3.9

(bottom) shows ray-tracing simulations of spectra from a 6 mm length of the 1 μm diameter FEL beam in a sample for two different photon energy regions, 260 eV and 550 eV. Double spectral lines demonstrate resolution capabilities. Also shown is the spatial resolution along the FEL beam for different lengths of the cylindrical mirror as the imaging errors increase with mirror length. The total length of the instrument is about 1.8 m. The 0.7 m of the instrument closest to the source point is merely a vacuum tube (Figure 3.3.10), which offers flexibility with respect to mounting the instrument on the experiment chamber. The time resolution is at best 30 fs in the centre (for 10 μm detector resolution), decaying off-centre to 300 fs at 0.5 mm, and 500 fs at 1 mm.
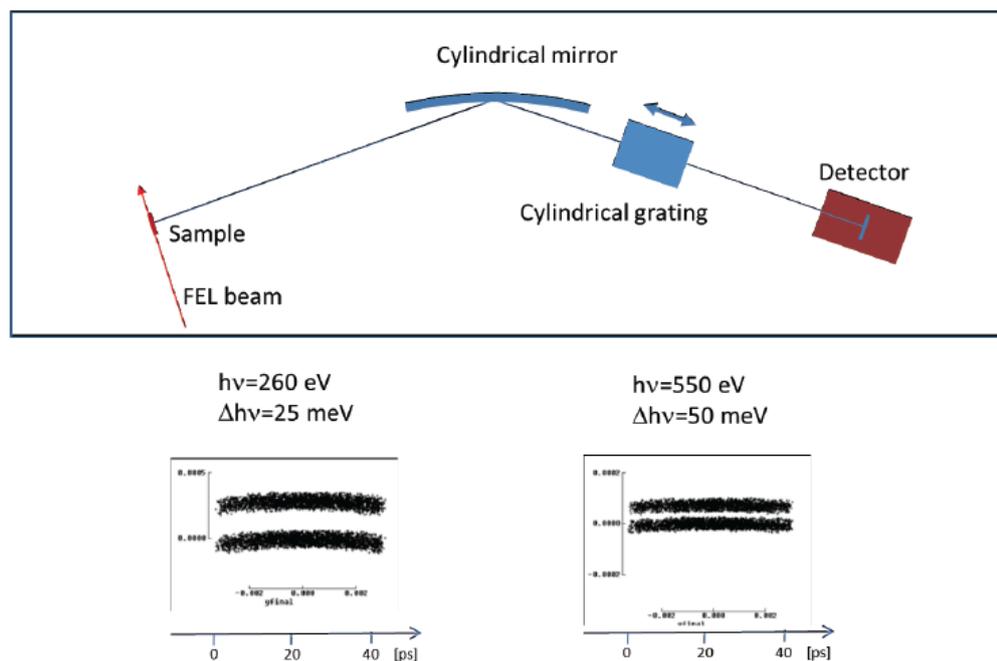
Figure 3.3.9: Top: *Schematic view of the 1D imaging XUV spectrometer.* Bottom: *Ray-tracing simulations of emission spectra for a 6 mm long intersection of a sample with a 1 μm diameter FEL beam for photon energies of 260 and 550 eV.*

A particular challenge for exploiting the full capability of the spectrometer lies in finding a suitable 2D detector with high spatial resolution and high readout speed. For application as a standard (non-imaging) X-ray spectrometer, the use of a Gotthard detector (see below) can be envisaged.
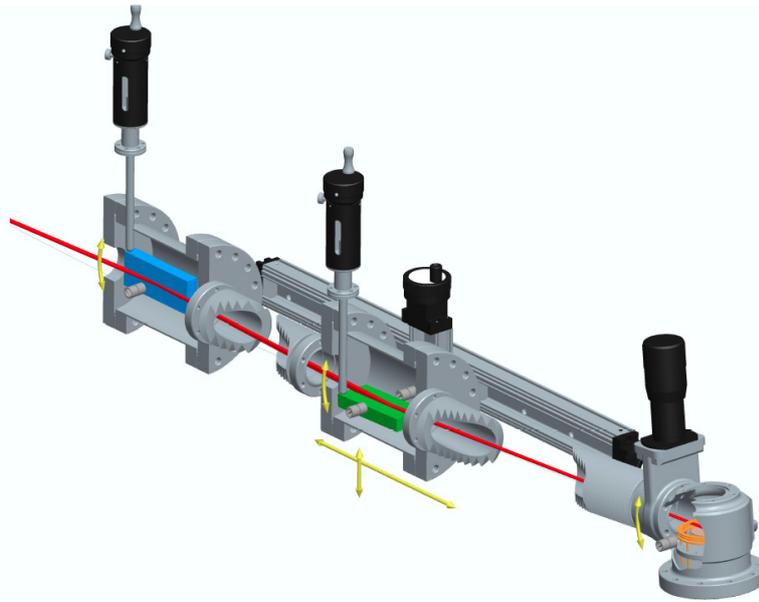
Figure 3.3.10: *Sketch of the 1D imaging XUV spectrometer. Distance from source to imaging cylindrical mirror (blue): 940 mm; radius of cylindrical grating (green): 20 m; movement of grating: 450 mm x 10 mm; groove frequency of grating: 600 /mm.*

3.3.1.4 Magnetic-bottle electron spectrometer (MBES)

The magnetic-bottle electron spectrometer (MBES) is used for measurements requiring a high collection efficiency, which opens up the possibility to perform single-shot spectroscopy. This is particularly interesting for time-resolved studies where beside the signal the temporal delay between the pump and the probe pulse is also monitored for each individual event in order to extract the jitter between both sources. In addition, the high acceptance is of great advantage for coincidence experiments requiring the collection of (ideally) all fragments produced in the same event.

The MBES for the SQS scientific instrument is a Swedish in-kind contribution (R. Feifel, University of Uppsala). A 3D CAD drawing of a magnetic-bottle spectrometer is shown in Figure 3.3.11. The working principle of this device relies on the diverging magnetic field lines of the strong permanent magnet (~0.5 T), which is located close to the intersection of the FEL beam and the (gas) sample jet and creates a magnetic mirror for collecting essentially all electrons ejected from the ionization region. A solenoid surrounding the 2 m long flight tube generates a weak (~10 mT), homogenous magnetic field, which guides the collected electrons towards the MCP detector located at the

other end of the flight tube. A multi-hit DAQ system registers the arrival time of each electron with respect to the ionizing laser pulse. Retardation voltages may be applied at the entrance of the flight tube in order to enhance the energy resolution in particular for high-kinetic-energy electrons. The MBES relies on the same principle as the spectrometers constructed by John HD Eland at Oxford University [Phys.Rev.Lett. 90, 53003 (2003)].

The 2 m MBES will be installed opposite to the entrance of the XUV fluorescence spectrometer. It will be used in combination with an MCP detector. The overall parameters of the MBES are given in Table 3.3.5.

Figure 3.3.11: 3D CAD drawing of a magnetic bottle

Table 3.3.5: Principal characteristics of the MBES

Overall length	250 cm
Length of TOF	200 cm
TOF diameter	15 cm
Distance to interaction volume	5 cm
Detector type	MCP
Detector size	42 mm

The effect of the strong magnetic field on the performances of the other spectrometers in the section around the focus F1, which is separated by 39 cm from the section around F1', will be investigated carefully in simulations

and practical tests. For the operation of the XUV spectrometer, the magnet has to be moved out of the interaction region.

3.3.2 NQS chamber

The second chamber dedicated to the study of larger system is essentially equipped with:

- a sample delivery system,

- an imaging detector,

- a REMI-type spectrometer,

- an electron or ion time-of-flight spectrometer,

- a Thomson parabola.

These devices are installed around the focal point F2 located 4.188 m behind the centre of the HFM. The vacuum conditions in the NQS chamber are mainly limited by the imaging detector and are at best about 10^{-10} mbar, which is obtained by a set of four to five turbo-molecular pumps (700 l/s). The whole chamber can be adjusted with respect to the FEL beam and focus position, i.e. it can be moved in three perpendicular directions and tilted in two directions perpendicular to the beam. The imaging detector can be dismounted and placed at various distances of up to 2 m from the interaction volume.

A schematic view of the NQS chamber and its individual components is given in Figure 3.3.12 and Table 3.3.6. The mechanical design can be seen in Figures 3.3.13 a, b, c.
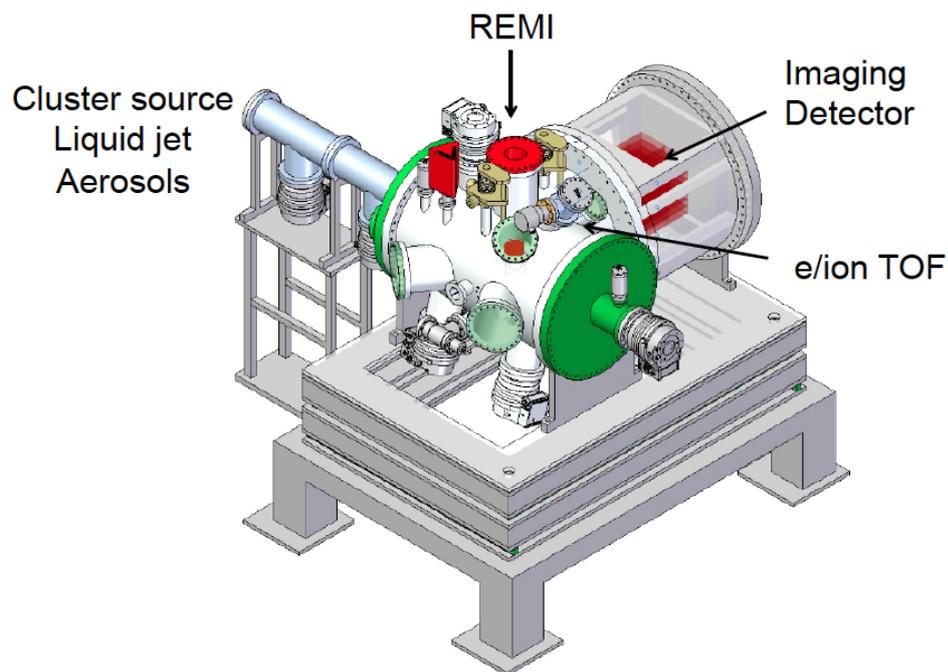
Figure 3.3.12: Schematic view of the NQS experiment chamber
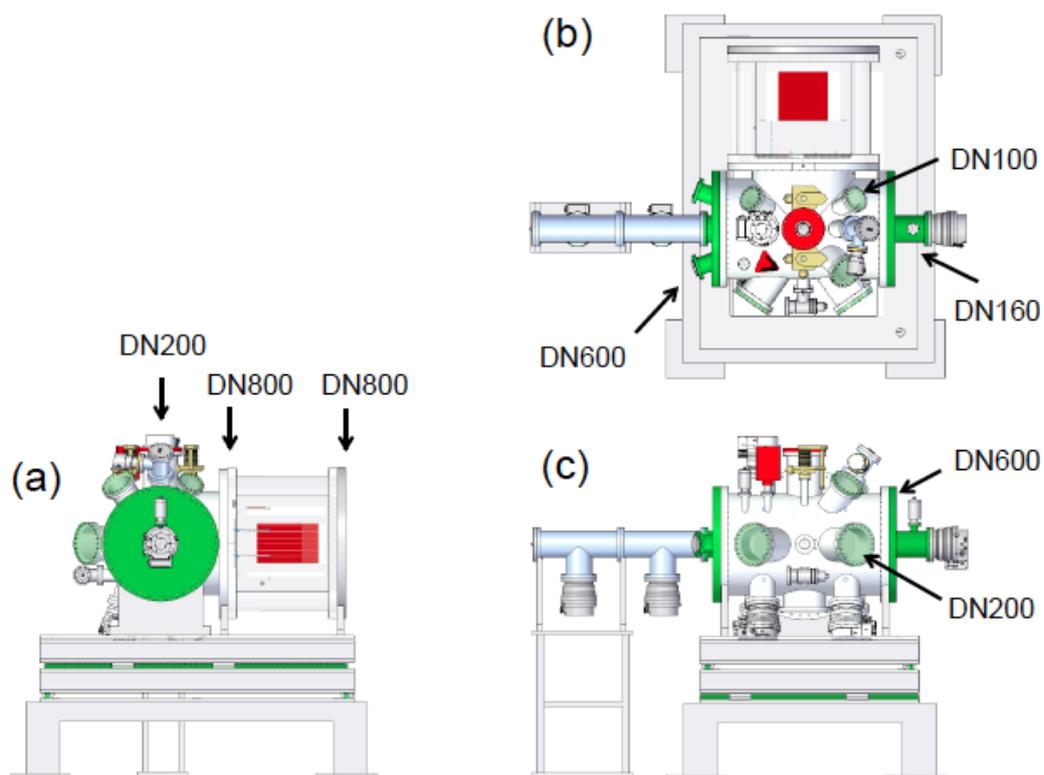
Figure 3.3.13: NQS experiment chamber: (a) side view, (b) top view, and (c) front view. Some of the principal distances and port size parameters are indicated.

Table 3.3.6: Spectrometers used in the NQS experiment chamber

Analyser	Acceptance	Resolution	Notes
REMI	4π	$E/\Delta E > 10^2$	angle-resolved, e–ion coincidence
Thomson parabola	< 1% of 4π	$E/\Delta E \approx 10^2$	High recoil energies
2D pixel detector	variable	< 5 nm	imaging, e–ion–photon coincidences
eTOF	5 % of 4π	$E/\Delta E > 10^3$	Sample characterization

3.3.2.1   Time-of-flight spectrometer (eTOF)

The electron/ion TOF is used to provide additional information on the fragmentation and relaxation processes taking place after interaction of the large samples with the intense FEL beam. The requirements are somewhat relaxed with respect to those defined for the AQS chamber in terms of spectral resolution. Therefore it is possible to choose a shorter overall length and a larger acceptance angle.

A design similar to that of Viefhaus et al. (2012) fulfils the main requirements (Figure 3.3.14). An MCP detector will be used for data recording.
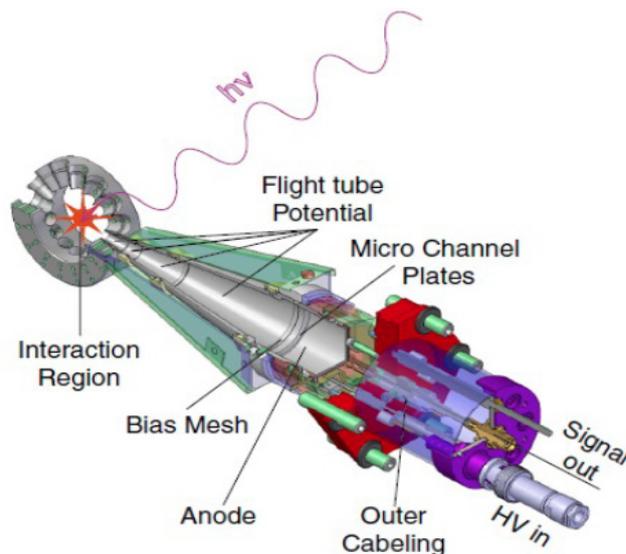
Figure 3.3.14: Design sketch of the high-efficiency eTOF spectrometer [Viefhaus et al., in preparation]

Table 3.3.7: Principal characteristics of the eTOF spectrometer

Overall length:	19.5 cm
Length of TOF	14.0 cm
TOF diameter	40.5 mm
Lens diameter	28.5 mm
Distance to interaction volume	few mm
Detector type	MCP
Detector size	28.5 mm

3.3.2.2 Thomson parabola spectrometer

A Thomson parabola spectrometer is used to measure the energy spectrum of different ion species in high-energy (keV–MeV) regimes. Magnetic and electric fields are used to deflect ions according to their velocity (v) and charge-to-mass (q/m) ratio.

The most basic design for a Thomson parabola ion spectrometer involves the use of an electric field, generated by a potential difference across a pair of electrodes, and a magnetic field, generated by either a pair of permanent magnets or a magnetic coil system (Figure 3.3.15). These fields are parallel to each other but perpendicular to the ions' initial direction of travel. For non-relativistic ions, the resulting ion dispersion, assuming uniform magnetic (B) and electric (E) fields, can be calculated as:

$$(3.5) \quad x = k \cdot \frac{ZeE}{mv_0^2}$$

$$(3.6) \quad y = k \cdot \frac{ZeB}{mv_0}$$

Where $k = L \cdot \left(D + \frac{L}{2}\right)$ is a constant depending on the geometry of the system.

Equations (3.5) and (3.6) are the parametric equations of a parabola in terms of v_0, and hence ions with distinct q/m form parabolic traces in the dispersion plane of the spectrometer (detector). The origin of the axes is defined by the projection of the two apertures on the detector plane. The distance from the

origin along one parabolic trace is a measure of the energy of the ions in the solid angle defined by the second aperture.
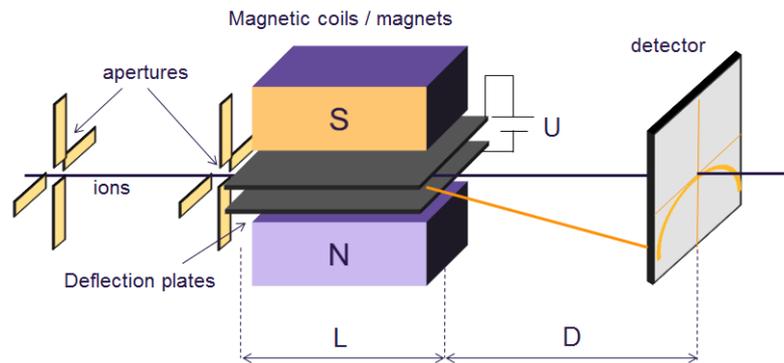
Figure 3.3.15: *Operation principle of the Thompson spectrometer. An imaging detector collects the ions. The two dimensions of the detector map the charge-to-mass ratio and the velocity (energy) of the ions simultaneously.*

Typical operation values for the E and B field are in the range of 10^5–10^6 V/m and 0.1–1 T, respectively. The dynamic range and resolution depend on the geometry of the spectrometer, the size of the detector (80 mm MCP plate with delay line / phosphor imaging detector is foreseen) and on the E and B settings. The resolution is also limited by the size of the entrance aperture of the spectrometer, as its projection at the detector plane defines the minimum separation required to resolve ions with different q/m and velocity.

Possibly, a design inspired by the modified scheme developed by Carrol et al. [NIMA 620 (2010) 23], featuring high q/m and energy resolution while keeping a compact size, can be implemented. The novel design utilizes a wedge configuration for the E field, in which the separation between the electrodes increases along the ion path. This is designed to produce a large E field dispersion and detectable energy range.

3.3.2.3 REMI-type spectrometer

A modified reaction microscope (REMI) spectrometer will be used to detect and analyse the electrons and ionic fragments, which are produced in the interaction of the nano-size objects with the intense XUV FEL beam. This REMI-type spectrometer is similar to the one designed for the CAMP chamber of the Max-Planck advanced study group [Strüder et al., NIMA 6124,

483 (2010)]. The specifically designed electrodes around the interaction volume will take into account the parallel measurements with the imaging detector (Figure 3.3.16). In this way, it will be possible to record electron–ion coincidences as well as fluorescence–electron–ion coincidences. The application as a reaction microscope for the complete determination of the fragmentation dynamics, which require the precise measurements of energy and momentum of all fragments arising from one molecule, is certainly limited (or even impossible) in this configuration, due to the specific design and, more importantly, due to the relaxed vacuum conditions imposed by the use of the imaging detector.

A combination of electric (few V/cm) and magnetic (some 10 Gauss) fields enable the measurement of the momenta of the electrons and ions that are produced in the photoionization process [Ullrich et al., Rep. Prog. Phys. 66, 1463 (2003)]. The overall length of the REMI will be about 40 cm. A pair of Helmholtz coils, which surround the whole chamber, will provide the magnetic guidance field.

In order to enable coincidence measurements, both sides of the microscope will be equipped with a delay line detector.
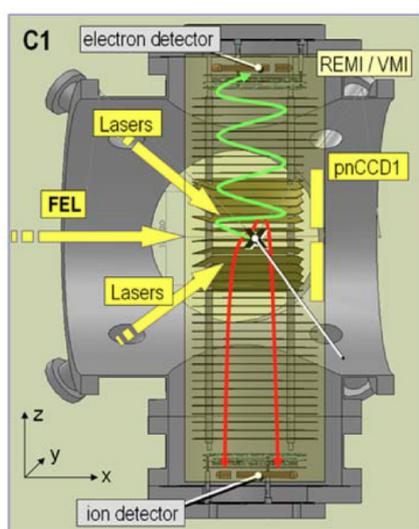
Figure 3.3.16: Schematic view of the REMI setup used in the CAMP chamber at LCLS and FLASH [Strüder et al., NIMA 6124, 483 (2010)]

3.3.2.4 Burst-mode compatible large-area imaging detectors

DEPFET sensor with signal compression – DSSC

The main component for all imaging experiments is the 2D megapixel imaging detector. In order to take advantage of the high repetition rate available at the European XFEL (max. 27 000 pulses/s), the development of the DEPFET sensor with signal compression (DSSC) detector was started (Figure 3.3.17). The DSSC detector [Porro et al., NIM A624, 509 (2010)] is dedicated to the soft X-ray regime and can record up to 600 images per bunch train. It consists of four modules with a 512 x 512 pixel area. The individual pixels are of hexagonal shape and have a size of 236 x 272 μm^2. The main performance characteristics of the DSSC detector are summarized in Table 3.3.8.
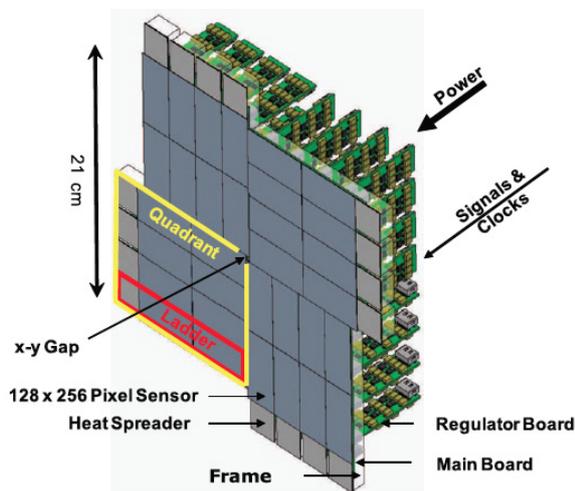
Figure 3.3.17: *Conceptual drawing of the DSSC detector illustrating the sensor geometry and arrangement of the front-end electronics [Porro et al., 2010]*

Table 3.3.8: *Performance parameters for the DSSC detector [DSSC consortium, priv. comm.]*

Energy range	0.25 – 6 (25) keV
Detector size	21 x 21 cm^2 1024 x 1024 Pixel
Pixel size	236 x 272 μm^2
Gap size (active area)	Minimal: 4.08 mm x 3.07 mm Maximal: 44.08 mm x 29.07 mm
Dynamic range	> 6000 photon/pixel/pulse at 1 keV
Single-photon sensitivity	5σ at 1 keV (5 MHz) 5σ at 0.5 keV (≤ 4.5 MHz)
Number of storage cells	576
Readout frequency	10 Hz

It is foreseen to provide an adjustable central hole for the detector with a minimum diameter of 2 mm (horizontal) and 2.5 mm (vertical) and a maximal opening of 42 mm (horizontal) and 29 mm (vertical) in order to adjust the "open area" of the detector to the FEL beam diameter when mounted at different distances to the interaction volume. Depending on the spatial resolution required for the investigation of an object with a given size, the detector has to be installed at a certain distance form the interaction volume. The minimum distance is 40 cm, determined by the dimension of the NQS chamber. The maximum distance is about 2 m, determined by the space available behind the chamber.

Within this range, it would be possible to measure samples with an overall size of up to about 10 μm (Table 3.3.9). The FEL beam diameter has to be adapted accordingly in order to cover the full sample size, i.e. it must be two to three times larger than the sample. For calculating the distances given in the table, it was considered that the fringes in the diffraction patterns are measured with a minimal number of 4 pixels. By setting the detector at the optimal distance, it is possible to determine, using the DSSC detector (1024 x 1024 pixels), the structure of objects of 1 and 5 μm size with a resolution of 5 and 25 nm, respectively.

Table 3.3.9: Optimal FEL beam diameter and sample–DSSC detector distances for different sample sizes and photon energies

Sample size	FEL diameter	Resolution	Optimal distance target–detector [m]			
[µm]	[µm]	[nm]	0.5 2.5	1 1.2	2 0.6	3 keV 0.4 nm
< 1	1	1.5	**0.07**	**0.15**	**0.3**	**0.45**
1	3	5	**0.2**	**0.45**	**0.9**	**1.35**
3–5	10	25	**0.9**	**1.8**	3.6	5.4
10	30	50	**2.1**	4.5	9.0	13
20	50	100	4.3	9.0	18	27

From Table 3.3.9, it becomes obvious that the maximal sample size that can be studied at the NQS chamber using the DSSC detector at 2 m distance is about 10 µm using 500 eV photons. For larger samples and higher photon energies, the distances exceed the space limitations. But also for a 10 µm sample, the transmission of the sample in the XUV photon energy range imposes additional constraints. With respect to the transmission curve of 10 µm carbon (Figure 3.3.18), it is clear that a required transmission of about 10% or more is only achievable for photon energies beyond 1000 eV.
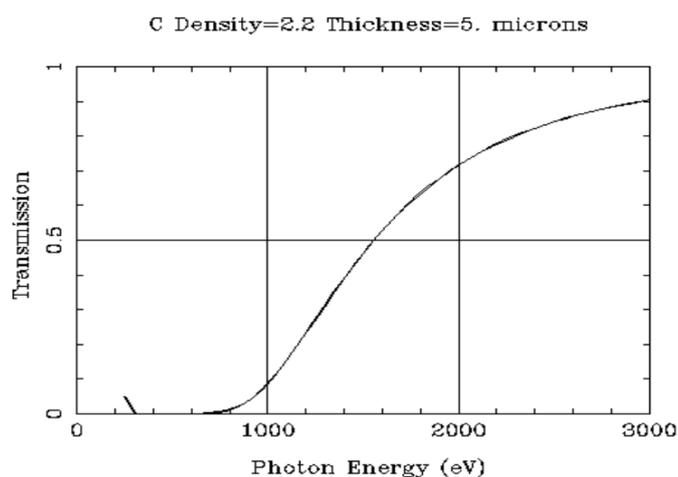
Figure 3.3.18: Transmission as a function of photon energy for a 10 µm carbon sample

As a consequence, for the investigation of larger samples at the SQS scientific instrument, other detectors with smaller pixel sizes have to be used.

Large-area imaging detector for low-repetition-rate applications

As alternative to the DSSC detector described in the previous section, we are considering CCD-technology-based imaging systems for Day-1 operation. Due to limitations of the readout speed, CCDs can be used for applications that do not require single-shot or pulse-to-pulse resolution. At present, we are considering two different technologies for these kind of applications, a CAMP-like 1 Mpx pnCCD developed at the Max-Planck semiconductor laboratory in Munich [Strüder et al. 2010] and a 2 Mpx Fast CCD presently under development at LBNL [Denes et al., Rev. Sci. Instrum. 80 ,8, 3302 (2009)].

pnCCD detector

The pnCCD sensor shown in Figure 3.3.19 [Strüder et al. NIM A 614, 483 (2010)] provides a smaller pixel size of 75 x 75 μm^2, enabling an extended range of sample sizes to be studied (see Table 3.3.10).
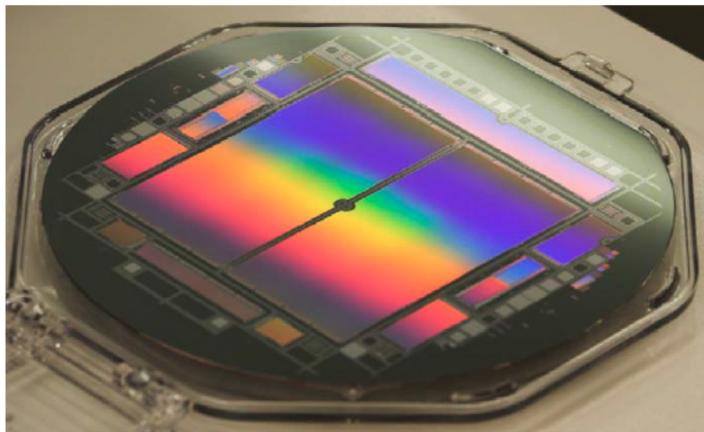
Figure 3.3.19: Photograph of a pnCCD sensor wafer without readout electronics and mechanical components. The two sensitive sensor areas with a size of 512 x 1024 pixels are clearly visible as large rectangular areas. The hole in the centre of the device provides sufficient space for the not-scattered central beam to pass through the sensor [Strüder et al. 2010].

Table 3.3.10: Optimal FEL beam diameter and sample–pnCCD detector distances for different sample sizes and photon energies

Sample size	FEL diameter	Resolution	Optimal distance target–detector [m]			
[µm]	[µm]	[nm]	0.5 2.5	1 1.2	2 0.6	3 keV 0.4 nm
< 1	1	1.5	**0.02**	**0.04**	**0.06**	**0.12**
1	3	5	**0.06**	**0.12**	**0.25**	**0.36**
3–5	10–15	25	**0.3**	**0.6**	**1.2**	**1.8**
10	30	50	**0.6**	**1.2**	2.4	3.6
20	50	100	**1.2**	2.4	4.8	7.2

The pnCCD detector consists of two halves of 512 x 1024 pixels each with a variable opening between both detector parts. The readout frequency is limited to 200 Hz at maximum, i.e. it is ideally suited for operation e.g. at LCLS (120 Hz), but would reduce to 10 Hz when using the particular bunch patterns at the European XFEL. The relevant performance parameters for the pnCCD detector are summarized in Table 3.3.11.

Table 3.3.11: Performance parameters of the pnCCD detector [Strüder et al. 2010]

Energy range	0.05–25 keV
Sensor size	7.7 x 7.7 cm^2 1024 x 1024 pixels
Pixel size	75 x 75 µm^2
Gap size	1–45 mm
Dynamic range	> 6000 photon/pixel/pulse at 1 keV
Single-photon sensitivity	5σ at 1 keV (5 MHz) 5σ at 0.5 keV (≤ 2.5 MHz)
Frame rate	Up to 200 Hz

Fast CCD

A further decrease of the pixel size is possible by using a Fast CCD, which is available from LBNL at the beginning of 2013 [Denes et al., Rev. Sci. Instrum. 80 ,8, 3302 (2009)] (see Table 3.3.12).

Table 3.3.12: Performance parameters of the LBNL Fast CCD detector [J. Joseph, LBNL priv. comm. March 2012]

Energy range	0.3–10 keV
Detector size	2.9 x 5.8 cm^2 916 x 1920 pixels
Pixel size	30 x 30 µm^2
Gap size	fixed-size central hole
Dynamic range	10^4, 10^3 > 500 eV
Single photon sensitivity	5σ at 0.5 keV (noise = 90 eV rms*)
Frame rate	200 Hz in 1k x 1k mode

3.3.2.5 Detectors for spectroscopic applications

1D strip detector

A candidate 1D detector – to be used as spectrometer detector for science and beam-monitoring purposes – is the Gotthard detector [Mozzanica, J.Instrum. 7 (01), C01919 (2012)], a silicon strip detector with small strip pitch (50 µm), which in its present development status can work at a maximum frame rate of 1 MHz. The summary of the present detector specifications is given in Table 3.3.13. Some modifications will be needed in order to be able to run the detector in vacuum and at the energies foreseen at the SQS station. Further development is required to increase the frame rate to 4.5 MHz.

Table 3.3.13: Performance parameters of the Gotthard detector [Mozzanica 2012]

Energy range	3.5–20 keV
Detector module size	6.7 x 13 cm^2
Module active area	64 x 10 mm^2
Pixel pitch	50 µm
Dynamic range	10^4 12 keV photons
Single-photon sensitivity	at minimum energy of 3.5 keV
Frame rate	> 50 kHz (continuous), 1 MHz burst

4   SQS instrument control system

The SQS experiment station control system (or instrument control system – ICS) has the purpose of configuring, operating, and monitoring the experiment hutch hardware and software, including vacuum, movements, voltage or current setting, and the data acquisition system (DAQ).

The criteria behind the design of the SQS-ICS are:

1   Realization of a common framework with the beamline control system, the undulator control system and the control systems of the other scientific instruments. This framework is being developed by the DAQ and Control Systems group (WP76). It is intended to be as versatile as possible, so that within the specific requirements of the SQS Instrument, the basic development concept as well as the software and the standard device and hardware models can be shared to help ease of operation and interchangeability of spares.

2   Realization of a system that can be remotely controlled as much as possible within the frame of a TCP/IP network. This feature allows the creation of a homogeneous user interface protocol for all the different devices within the instrument; it allows us moreover to reduce the distance between the device and the accessory hardware. In the case of DAQ devices, this is a main point in reducing the sources of electronic noise that degrade the quality of the measurement.

3   Possibility to develop a robust and versatile standard for implementing data quality monitoring (DQM) for all the data acquisition systems of the instrument.

4.1 Control system architecture

A schematic representation of the control system architecture is shown in Figure 4.1. The core element in the system is the programmable logic controller (PLC) unit. Each device in the instrument that needs to be monitored and controlled is connected to a PLC within a local network. The PLC is a program running on one or more devices and is implemented on a CPU server with a real-time operating system (RTOS).
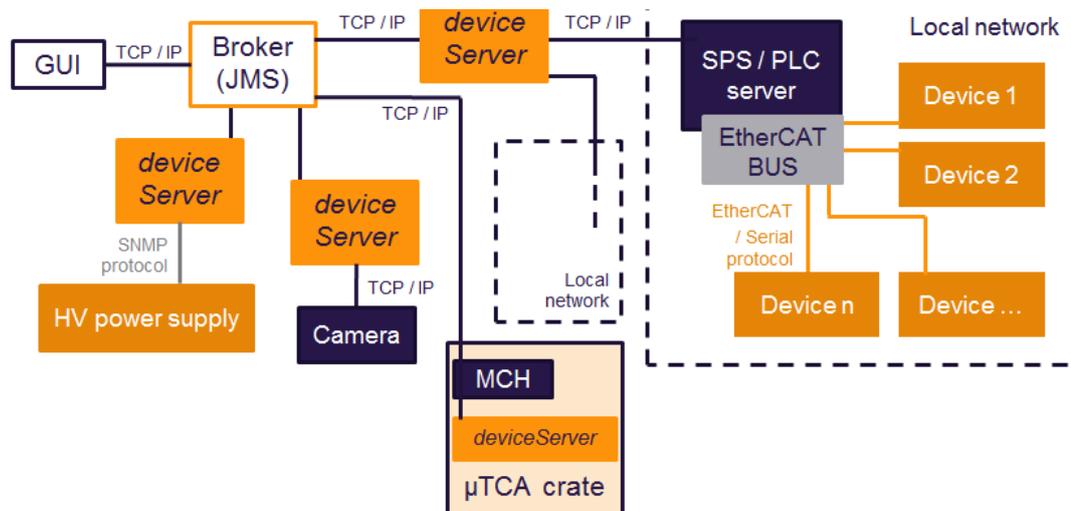
Figure 4.1: Block diagram of the instrument control system (ICS) displaying the interconnection between different elements

The RTOS ensures that the server will elaborate (and respond coherently to) the feedback from the device(s) within its operation cycle, which according to the complexity and the need of the operation performed by the device, the CPU performance, and the number of devices within the local network is typically set between a fraction of a millisecond and a few milliseconds. The connection protocol within the local network is the EtherCAT fieldbus system. To be supported within this framework all devices (including external user devices) need to have an EtherCAT-compliant interface or a serial interface with completely open protocol. Motors may be equipped with an encoder, as needed.

The PLC is controlled via a program called deviceServer, which is run on a Linux host. Each host may be connected to one or more PLCs where a

TCP/IP server is running. Each deviceServer runs as many devices as the number of hardware devices physically attached to the PLC; it interfaces the PLCs to the users, provides PLC changes of configuration, logging, archiving, and messages other deviceServer units to establish the needed inter-communication.

The messages from all deviceServer units are managed by a provider or broker (Figure 4.1), which also manages the interface between the deviceServers and the graphical user interface (GUI).

Within this framework, the GUI can be extremely essential, as it does not need, per se, to contain any business information about the actual number or nature of the devices it is connected to. These pieces of information are injected at runtime. This makes the system extremely flexible with respect to the effective needs of the users.

In the SQS Instrument, there are essentially five classes of devices that will be controlled within this framework:

1 Vacuum Hardware: pumps, gauges;

2 Positioning hardware: motors, encoders, end switches;

3 High-voltage and high-current power supplies;

4 Low repetition rate DAQ: cameras, spectrometers, etc.;

5 High repetition rate DAQ.

Devices and parameters relative to classes 1–4 are briefly discussed in the following. The DAQ system architecture for high repetition rate (MHz) measurement processes, implemented within the frame of the MicroTCA (µTCA) standard, is discussed in more detail in the next section.

4.1.1   Vacuum hardware

The vacuum chambers of the SQS scientific instrument (AQS, NQS, KB system, diagnostics devices) are pumped by approximately 20 turbo-molecular pumps, 8 ionic pumps and 15 primary pumps, with a total maximum power consumption of approximately 30 kW. The vacuum is

monitored by three classes of vacuum gauges (hot cathodes, cold cathodes, Pirani gauges). Redundancy for critical vacuum measurements is envisaged.

Both vacuum pumps and gauges are controlled via serial ports / RS232 with an open protocol, compatible with the control system architecture.

The interlock system for the safe operation of shutters can be completely configured via software within this frame; where possible, digital or analogue signals will be used.

4.1.2   Positioning hardware

Many parts of the experiment station need to be positioned with different levels of resolution, dynamic range, and vacuum compatibility. Both translational and rotational movements are needed, in particular (degrees of freedom (DoF), vacuum compatibility, and resolution/dynamic range indicated):

- ■ **Translation and rotation/tilting:**

    — experiment chamber positioning (5 DoF, atmosphere, 1 µm/20 mm,

    — 10 µrad/5°);

    — TOF spectrometers pointing (3 DoF, atmosphere, 10 µm/10 mm, 10 µrad/2°);

    — molecular/cluster jet pointing (3 DoF, vacuum, 10 µm/50 mm,

    — 10 µrad/2°);

    — KB mirrors (6 DoF, vacuum, 10–100 µm/50–500 mm, <1 µrad/5 mrad);

- ■ **Translation:**

    — beam slits (UHV, 10 µm/10 mm),

    — XUV spectrometer slits (UHV, 1 µm/2 mm),

    — Thomson parabola slits (UHV, 10 µm/5 mm);

    — beam position monitor screens (UHV, 1 µm/10 mm);

— optical laser beam collimation [lenses/telescopes] (atmosphere, 10 µm/100 mm);

— shutters (UHV atmosphere, ON/OFF);

■ **Tilting/rotation:**

— laser beam steering (UHV atmosphere, <1 µrad/10°),

— optical laser waveplate positioning (atmosphere, 1°/360°);

Most of the movement requirements are attainable with stepped motors equipped with encoders. For some high-precision movements like e.g. optical beam steering mirrors, a specific solution for integrating piezo-driven motors should be studied.

4.1.3   Power supplies

High-voltage and high-current power supplies are needed for the electron and ion spectrometers (electrodes, MCP) and accessory tools. Typical voltage settings need to be up to 6 kV, limited to 1–3 mA. For a particular application (high kinetic energy VMI), the voltage of the electrodes needs to be set up to 20 kV, with negligible drain current. Helmholtz coils typically require currents in the range of 2–10 A.

For eTOF–VMI coincidence measurements, where the VMI is performing ion imaging in coincidence with energy-resolved electrons detected by a TOF, the VMI electrodes need to be pulsed. Typical pulsing voltages are on the order of a few hundred volts. The ideal pulsing device is featuring low (1 ns or below) rise time, adjustable on-time, and low (tens of ns) recovery time in order to enable MHz burst frequencies compatible with the European XFEL timing structure. Besides a proper selection of the HV pulser, a careful design of the passive element circuit is needed.

Sample delivery devices (piezo-valves and solenoid valves) need pulsed power supplies to be triggered by the 10 Hz from the FEL. Working voltages are in the range of a few hundred volts.

4.1.4 Low repetition rate DAQ

A class of devices implemented in the SQS instrument do not give the possibility to exploit the burst timing structure of the European XFEL, being limited in their triggering possibilities to the 10 Hz inter-burst repetition rate. These include:

■ Most of the optical laser diagnostic tools: fibre optic spectrometer, frequency-resolved optical gating (FROG) spectrometer, power meter;

■ The CCD cameras included in the VMI and XUV spectrometers;

■ The CCD cameras enabling FEL beam diagnostics (pointing monitor).

The camera-based devices are interfaced to dedicated deviceServer units via Ethernet connection or to their own PC via CameraLink, according to the model of the camera. Specific solutions have to be studied for the FROG spectrometer, which is normally run by a Labview driver in a Window environment, and the power meter, for which so far only a solution with a general purpose interface bus (GPIB) connection, not complying with the WP76 standards, is available.

4.2 DAQ system architecture

The DAQ on the intra-burst (MHz) repetition rate is implemented within a MicroTCA (μTCA) framework. The μTCA standard is a part of the telecommunications computing architecture (TCA) standards defined by the PCI Industrial Computer Manufacturers Group (PICMG) defining an architecture for high-performance, high-density, packet-based systems focused on a smaller form factor chassis.

This standard is fully coherent with the philosophy behind the undulator, beamline and hutch control systems developed at the European XFEL and is adopted for controlling the machine as well. It provides a system that is

■ Compact, modular, and therefore easily customizable;

■ Completely controllable within a TCP/IP network from a remote location;

- Allowing the establishment of connections between the different modules with a wealth of high-speed connection protocols. This allows data transfer and online data analysis processes for an extremely broad range of I/O complexity.
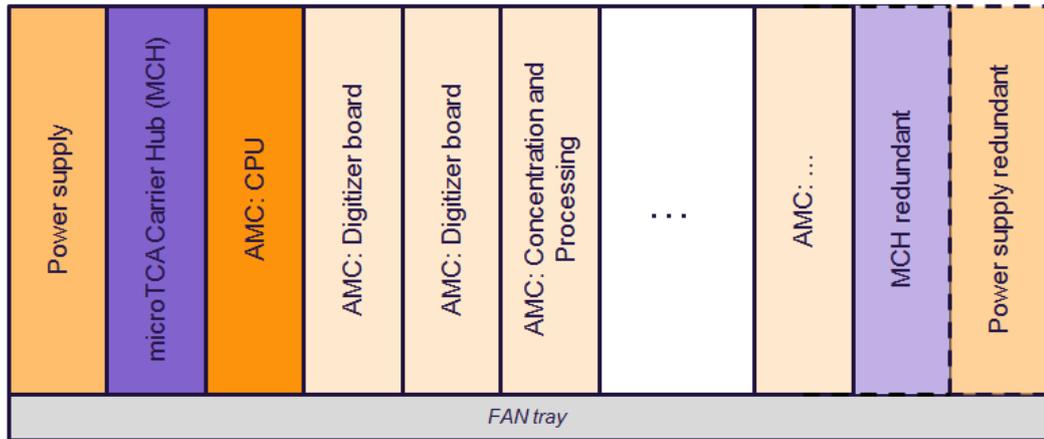
Figure 4.2: DAQ system architecture based on the μTCA standard

A schematic representation of a μTCA system is shown in Figure 4.2. The system consists of the following elements:

- A power supply module (possibly redundant) and a fan tray cooling unit (dissipating up to 80 W/board);

- At least one, up to two μTCA carrier hub (MCH) board(s) featuring:

  — Implementing all temperature sensor readings allowing for automatic warning and error report and switch-off in case of failure;

  — Controlling power supplies;

  — Incorporating the PCI express switching point;

  — Implementing a gigabit Ethernet switch for all modules providing an interface;

  — Distributing the standard clocks to all the AMCs without the need of hard cabling.

    The second MCH is for sake of redundancy; its presence is critical in the tunnel control system but can be dispensable for the ICS.

- From one to twelve advanced mezzanine cards (AMCs). AMCs are I/O boards complying with the Advanced TCA standards. In the SQS µTCA crates, they are of three types:

  — **Digitizer (ADC)** boards for the acquisition in digital form of the analogue traces from MCP and delay line detectors (described in more detail below);

  — **CPU boards** performing online analysis algorithms and streaming the processed data to further DAQ stages (PC layer/storage);

  — **Concentration and processing boards**, which are able to collect data of all digitizers and can do complex online processing with low latency, e.g. featuring data filtering. For memory-demanding concentration and online processing applications, the ATCA-based train builder DAQ modules could be used, which provide a common readout system for the 2D megapixel detectors. The flexibility of the framework can be exploited to make use of the high memory performances of this board also for other purposes.

Connection speed and protocols: Besides the connection of the modules with the in-crate CPU via the MCH PCI express switching point (at present speeds up to 8.5 Gbit/s times four lanes are supported), there are other possibilities of interconnection between the boards. Depending on the scheme of the backplane, point-to-point hardware connections without the need of MCH configuration (up to 12 Gbit/s foreseen) are possible. AMC boards are supported featuring optical 10 gigabit Ethernet (GbitE) external connections for linking to external boards; this interface is not a µTCA standard, but it is established as a standard for the European XFEL in order to allow flexible interconnects with different systems and hardware.

Analogue to digital converter (ADC) boards: The available digitizing resolution and dynamic range are 1.6–7 GS/s with 14–8 bit. The optimal resolution–dynamic range solution depends on the application and is going to be matched to the duration and amplitude of the pulse coming from the MCP and delay line detectors (see Section 3.3). All ADCs allow direct data streaming via 10 GbitE and feature online data processing within the included FPGA; maximum streaming speed between boards in the crate via the

backplane is 6.6 Gb/s. In perspective, ADCs boards with 30–40 GS/s speed / 8 bit dynamic range will possibly become compatible with the μTCA standard in terms of data streaming protocol implementing 10 GbitE ports, making it feasible to include them for very high time resolution measurements.

Online data analysis protocols: Processing of the data within their stream to the long-term storage is to be implemented for three main reasons:

- The possible need of providing additional information to the veto decision unit on a very (μs scale) short time scale via low-latency links;

- The requirement for a real-time (on the inter-burst repetition rate, 100 ms, scale) monitor of the output of the ongoing experiment to drive human decisions;

- The need to reduce the data before long-term storage due to the extreme large volume of the raw data, which makes the perspective of an integral storage unrealistic.

Performing online analysis on a μs time scale is made possible by the presence of an FPGA in each of the ADC boards and by the high connection speed within AMCs. WP76 is going to develop a Simulink interface to the FPGA firmware, to allow instrument scientist and users to develop their own online analysis codes in a user-friendly environment. The interface converts the algorithms into the original manufacturer language. For algorithms involving complex operations or large data amounts, the implementation of online analysis processes on other boards within the μTCA crate (CPU, concentration and processing boards / veto decision unit boards) or the external train builder is foreseen. The algorithms are going to be coded looking for the optimal trade-off between computation efficiency and accuracy, involving where needed and possible the use of lookup tables.

Among others, the following algorithms are going to be developed in collaboration with WP76:

- Constant-fraction discrimination (CFD) / pulse COM determination in analogue 1D trace for event counting purposes;

- Centroiding algorithm for single-particle detection on an CCD detector;

- Inversion algorithm to retrieve electron energy and angular distributions from VMI measurements (onion peeling, Abel inversion);

- Hex-Anode delay line detector event reconstruction;

- Covariance mapping for revealing hidden correlations between different signals via a shot-by-shot analysis [Frasinski et al, Science 246, 1029 (1989)];

- Treatment of multi-ion–multi-electron coincidences discriminating random coincidences on a statistical basis [Prümper and Ueda, NIMA 574, 350 (2007)].

Too complex algorithms might take several tens of µs and thus would not be usable to provide vetoing to the data acquisition. As long as a bunch train can be processed and data transferred within the inter-burst period of 99.4 ms, the algorithms remain effective for online monitoring and pre-storage processing purposes.

5 Sample delivery

5.1 Molecular beam

A conventional molecular-beam apparatus will be installed as standard gas delivery system at the AQS experiment chamber. In order to match the 10 Hz pulse train structure of the European XFEL and to decrease the gas load in the experiment chamber, a pulsed piezo valve and a differential vacuum system will be installed. The valve should be operated for opening time up to ~2 ms to match the full bunch duration (600 µs) with a smooth enough flowing condition corresponding to a ~2% duty cycle. The pumping speed needed for the expansion chamber will be ~5000 l/s, to be provided by 2 x 2500 l/s turbo-molecular pumps. A cooling system for the beam nozzle, intended for the generation of rare-gas clusters, will possibly be included. For other clusters, like metal clusters, a specific system has to be built. It is part of the add-on equipment, which is provided by interested user groups.

5.2 Liquid jet

The liquid-jet assembly is a development of the Sample Environment group (WP79) based on the design concept of M. Faubel, Microliquids GmbH. It consists of a convergent quartz glass nozzle, which is fixed in a custom-made PEEK holder and connected via a capillary tubing to a high-performance liquid chromatography (HPLC) pump, which drives the liquid jet typically at pressures of 10–50 bar, providing jet flow speeds up to 120 m/s.

The liquid-jet diameter can be chosen freely in a range from approximately 5 to 200 µm. The lateral jet stability is better than 1 µm at 1 mm distance from the nozzle exit. The maximum length of the uninterrupted cylindrical section of the liquid jet is 3 mm for 5 µm diameter jets. It increases rapidly with

increasing jet diameters (reaching 20 mm length for 15 μm jets). Narrower jets down to 2 μm diameter have been made with this system. Lower jet diameters need more development for stable working. A broad range of solvents can be used for jet operation, even volatile and viscous solutions. Precautions should be taken with very corrosive materials.

The liquid-jet solution is returned through a narrow beam catcher aperture, which improves the vacuum and allows for re-usage of the material. Heating of the catcher aperture helps to prevent ice formation.

In a vacuum chamber with circa 1500 l/s turbo-molecular pump capacity and using an additional, liquid nitrogen filled, 2 l volume hang-down cryotrap, a vacuum in the 10^{-5}–10^{-6} mbar range is reached for water micro-jets.

Figure 5.1 shows a sketch of a compact liquid-jet setup (Microliquids GmbH) with a liquid micro-jet and the beam catcher unit. The motors for *xyz* motion for the whole setup and for the *xyz* motion of the micro-jet relative to the beam catcher are integrated in the vacuum chamber. The technical design of the injector will be optimized and adapted for use in the NQS chamber at the SQS scientific instrument. The design will take into account requirements of flange sizes and distances as well as necessary space restrictions.
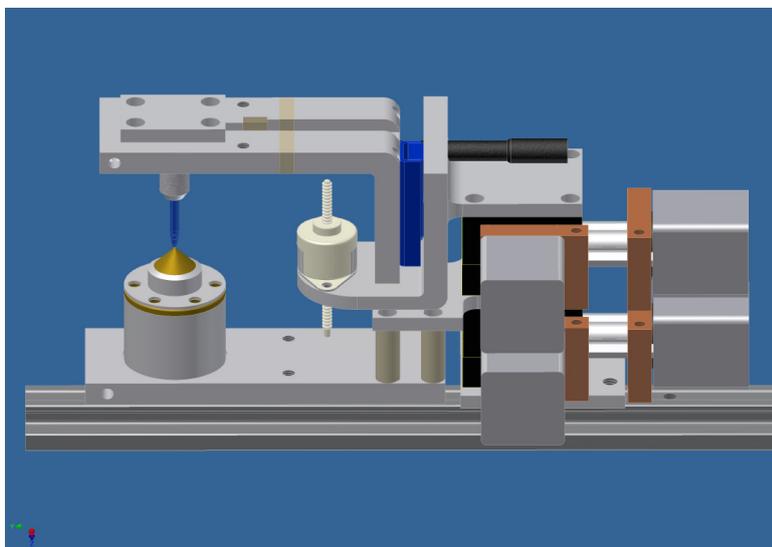

Figure 5.1: Scheme of the compact liquid-jet setup (Microliquids GmbH)

5.3 Controlled molecular beam setup (COMO)

The COMO setup consists of a doubly differentially pumped vacuum system with a source chamber containing the molecular-beam source, a first skimmer for differential pumping, a second vacuum chamber housing the selector, and another skimmer for differential pumping towards the end station. The design of an equivalent setup provided for the CAMP end station at LCLS is shown in Figure 5.2. The system can be placed at any distance from the interaction point, using for example an inverse flange. The molecular-beam valve is easily changed and different options will be explored to provide optimal conditions for the various operation rates (molecular-beam rate: single-shot 10 Hz, burst mode, long-pulse 10 Hz, continuous beam), i.e. an Even-Lavie solenoid valve, a cantilever piezo valve, and other (commercial) pulsed gas valves and continuous nozzles. In the original COMO setup, we envision to provide the following molecular-beam nozzles and valves:

Figure 5.2: *Design of the controlled-molecules setup for CAMP at LCLS provided by Küpper et al. (CFEL Hamburg). The large flanges are DN 250 CF in this particular setup and the measures given in the figure are in millimetres.*

5.3.1 Even-Lavie valve

This valve can operate in single-shot 10 Hz mode producing quite intense and extremely cold beams (<1 K). It will have minimal pumping requirements.

5.3.2 General valve Series 9

This valve can operate in 10 Hz long-pulse mode (up to opening times of some ms) at moderate stagnation pressures producing dense cold initial beams (<2 K). It entails considerable pumping requirements (some thousand l/s at 10^{-5} mbar).

5.3.3 Piezo valves

These valves can operate in long-pulse mode with the same characteristics as the general valve system. Moreover, they can be used in CW mode, yielding considerably colder beams at lower density and also, in that mode of operation, entailing much higher pumping requirements ($\approx$10 000 l/s at 10^{-5} mbar). It might also be possible to operate piezo valves in burst mode, i.e. during the European XFEL burst. This fits also to the laser systems proposed by the Optical Lasers group (WP78), where 1 ns pulses of some 10 mJ should be available at these rates as well, allowing the creation of strongly adiabatically aligned samples. However, this mode of operation has not yet been tested and is therefore not considered as part of the standard COMO setup at present.

5.3.4 Continuous-beam nozzle

A simple continuous-expansion nozzle allows the production of moderately dense, very cold initial beams at the cost of very high pumping requirements, as is the case with the piezo valves in CW mode. It is, however, an extremely simple setup. Moreover, it will be easily possible to exchange the valve against other sources – developed over the next years – producing cold beams within the COMO setup. For experiments using the European XFEL in single-bunch mode at 10 Hz, pumping requirements are minimal. For experiments in continuous-beam operation or in pulsed operation with long pulses covering all (or a large fraction) of the micro-pulses in the European XFEL bunch, the pumping requirements are demanding. We envision to provide 6000 l/s (at 10^{-5} mbar) pumping speed in the source chamber and >1500 l/s (at 10^{-7} mbar) in the selector chamber. This setup – including the second differential pumping stage – will allow pressures of <10^{-9} mbar in the interaction volume during operation. If better requirements are necessary, a beam dump opposing the molecular-beam source could be implemented if space (inside and around the end station) is available.

5.4   Nano-particle source

An aerosol sample injector and catcher system is available for sample injection at the NQS chamber. The source is being developed at the University of Uppsala (J. Hajdu et al.) and permits the injection (and subsequent capture) of single aerosol particles into the pulsed beam of the FEL. The current prototype (Mark III) can focus particles of 3–3000 nm diameter into a spot of a few µm. A diameter of 15 µm has been measured during experiments at the CXI station at LCLS. The luminosity of this aerosol injector significantly exceeds that of other aerosol injectors and matches the luminosity of currently available liquid-jet injectors (without the background signal from the excess liquid). Hit rates on 0.7 µm biological objects (viruses and cells) reached 43% during trials at the LCLS (3–5 µm X-ray focus).
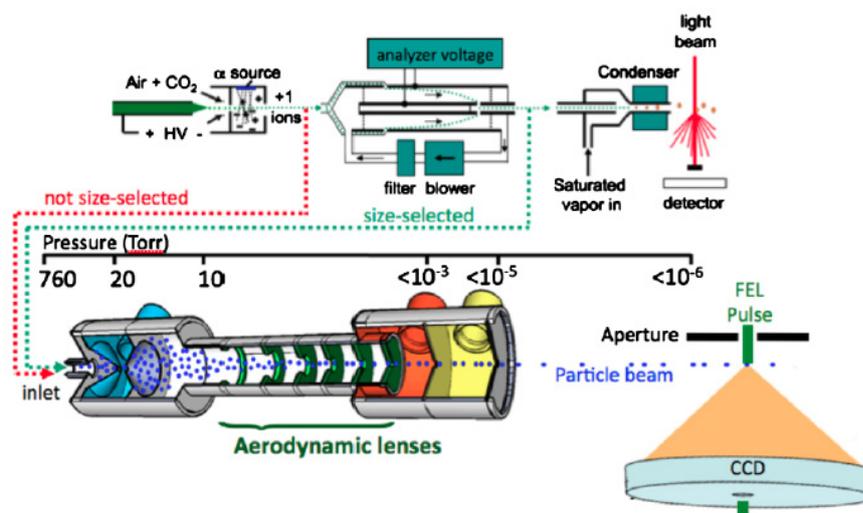
Figure 5.3: *Scheme of the aerosol sample injector [Bogan et al., Phys. Rev. Spec. Topics 13, 094701 (2010)]*

The scheme of the source is given in Figure 5.3. The aerosols are injected via an aerodynamic lens stack into the vacuum system. Generally it is possible to use different types of aerosol sources, such as nebulizers, atomizers, flames, and dispersion of dry powders.

The injector design aims for best possible performance for particles in the range from 10 to 600 nm. In close contact with WP79, the technical design of

the injector will be optimized for use in the NQS chamber at the SQS scientific instrument. The design will take into account requirements of flange sizes and distances, as well as necessary space restrictions. Special attention will be given to ensure that a sufficient opening angle for the scattered X-rays is provided.

The injector design includes a particle catcher. The catcher efficiency should be such that there is no observable contamination from the injection on the camera or chamber interior after one week of normal injector operations. The injector system also includes a laser-based system for alignment.

The possibility and necessity of passive and active alignment systems will be explored. By means of static engineering, the best passive stabilization method for the injector system will be developed. A prototype of a laser-based injector has been built in Uppsala. This system can be the basis for developing an active feedback system. Such a system could maintain high hit rates for prolonged times. If an active position feedback system promises to be beneficial in the test phase, the final injector system will be equipped with such a system.

A new particle catcher will be developed to guide injected particles that missed the European XFEL beam out of the vacuum chamber and then dump them safely. This is particularly important with potentially dangerous aerosols, such as most biological aerosols.

Alignment of the injector to intersect the FEL beam can be performed with a laser beam that passes through the injector and then intersects the FEL beam. The ability to send a laser beam (or laser pulse) with any desired polarization down the injector during operation opens up new opportunities to guide, orient or excite particles along the injection line, and synchronize the optical laser pulses with any desired phase shift relative to the European XFEL pulses.

6 SQS optical laser handling

Optical-laser (OL) radiation is delivered to the SQS experiment station for performing experiments based on the combination of the ultrashort and intense FEL pulses with an additional synchronized fs/ps optical laser. Lasers with 800 nm and 1030 nm wavelength are under development. Running parameters for the laser system are summarized in Table 6.1.

Table 6.1: Optical laser working parameters

Purpose	Laser wavelength	Inter-burst frequency	Intra-burst frequency	Energy	Burst avg. power	Pulse duration
	[nm]	[Hz]	[MHz]	[mJ/pulse]	kW	[fs]
Pump-and-probe	800	10	1–4.5	1–0,2	1	15–100
Molecular alignment (I)	800	10	0.2	>3	1	<20
Molecular alignment (II)	1030	10	0.2	~100	20	10^3–10^6

The laser system fulfilling these requirements is presently being developed by the Optical Lasers group (WP78); its technical design is therefore not discussed here. This section presents the technical details of the OL operation within the frame of the SQS instrument, with focus on:

1   The OL-related baseline instrumentation, including beam properties control devices, beam steering devices, and OL diagnostics tools;

2   The coupling of the OL beam with the experiment station, including the design for FEL–OL spatial and temporal alignment.

The discussion here focuses on the 800 nm operation. For a certain class of experiments, the 1030 nm beam will be used. The design of its integration

into the SQS laser operation system is currently under development and is not discussed here.

6.1 Optical laser operation

A schematic representation of the layout for the OL-related baseline instrumentation and beam steering system from the laser hutch to the experiment chamber is shown in Figure 6.1. The elements of this layout will be arranged on two 3000 x 1250 cm^2 optical tables situated in a separated instrument laser hutch and, as needed, on additional breadboards placed close to the vacuum chambers. As discussed in Chapter 3, a separation (complying with radiation safety specifications) between the X-ray experiment hutch and the instrument laser-hutch is identified as a preferable solution, allowing for independent operation of the two sources in experiment preparation phases.
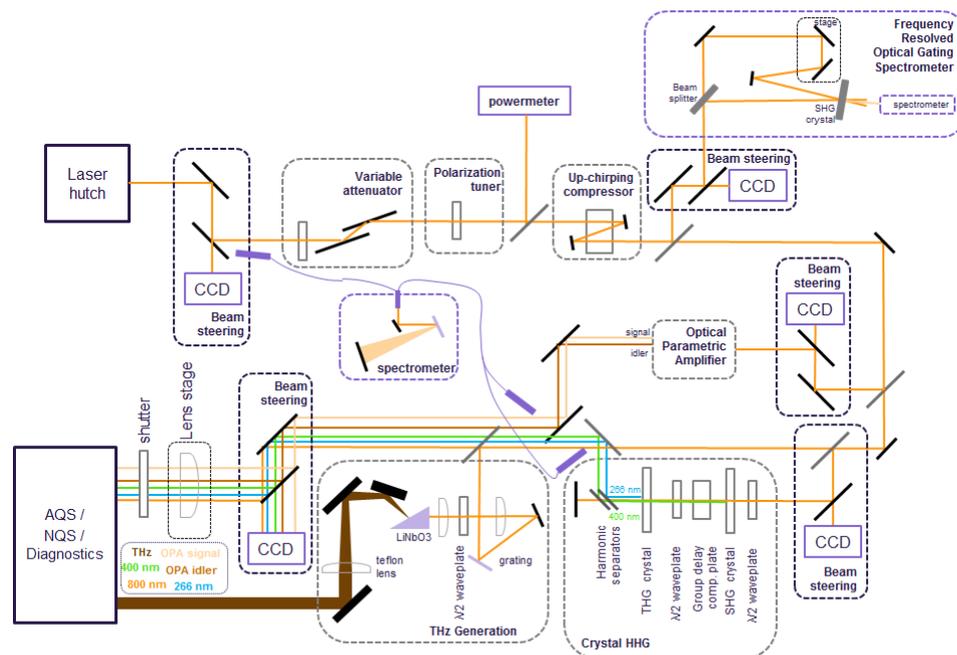
Figure 6.1: Tentative optical layout of the SQS laser operation system. Different colours are used to identify different categories of devices: control devices for beam properties (grey boxes), beam steering (black boxes), and monitor devices for beam properties and diagnostics tools (purple boxes).

The elements in the layout can be listed according to the categories mentioned above:

6.1.1 Beam properties control devices

- Beam intensity and polarization are controlled by encoded motorized rotation stages on which a λ/2 waveplate is mounted. Intensity is tuned by having the beam reflected by two thin-film polarizers (TFPs), which reflect only *s*-polarized light. Rotating the waveplate allows tuning of the beam intensity over a wide dynamic range (0.2–85% foreseen). The alteration of other beam parameters, which might be critical at the shortest (~15 fs) projected pulse duration, will be carefully considered.

- Beam pulse duration is tuned using an up-chirping compressor consisting of an optical path with variable length through fused silica, thanks to the negative chirp characterizing the stretched beam delivered by the laser hutch. A specific design for a variable compression effect is under development by WP78.

- For the 800 nm OL, the wavelength of the radiation delivered to the experiment can be controlled using an optical parametric amplifier (OPA); moreover, second-and third-harmonic (400 nm / 266 nm) radiation can be produced using non-linear crystals. Commercially available OPAs pumped with 20–300 fs, kHz, mJ mode-locked 800 nm laser radiation provide an output wavelength typically ranging from 1100 to 2600 nm; with optional frequency mixers, this range can be extended down to 189 nm and up to 20 μm, respectively. Conversion efficiency is >>10% in the standard wavelength range going down to < 0.1% if frequency mixers are used. Repetition rate regime and maximum average input power must be addressed within the development of the laser system.

- Ideally, a transform-limited input pulse of >25 fs duration is required for optimal conversion efficiency from OPA, second-harmonic generation (SHG), and third-harmonic generation (THG). This will possibly need a reconfiguring of the laser dispersion management, done in the laser hutch.

- Generation of THz radiation is foreseen for specific experiments and for FEL diagnostics purposes. In the layout drawn in Figure 6.1, a setup

based on tilted wavefront generation [H. Hirori et al., Applied Physics Letters 2011, 98 (9), 3], capable of producing extremely high fields in the THz pulse, is included as an example. Exploitation of other solutions including difference frequency generation in an organic crystal [Appl. Phys. Express 1 (2008) 042002] is foreseen.

6.1.2 Beam steering

Piezo and manually driven mirror mounts with < 1 µrad tilting precision steer the beam along the layout. Depending on the laser beam characteristics and pulse energy, 2" or 3" standard is adopted. Mirrors marked in grey in the representation of the layout (Figure 6.1) need to be inserted and removed from the optical path with a high degree of repeatability. A kinematic base with a ball and V-groove design is identified as a preferable solution in terms of repeatability (30 down to 1 µrad vs. 200 µrad) against a (motorized) flip mirror.

6.1.3 OL diagnostics tools

The OL beam is characterized in terms of intensity, position stability, spectral properties, and pulse duration (see Figure 6.1). A most critical issue, already addressed in the control system chapter, is the integration of the OL diagnostic devices with the instrument control system. For sake of representation, the temporal characterization is shown here right after the fused silica compressor. In the case of operation with very short (~15 fs) pulses, the transmission through all the following optical elements needs to be considered carefully. As a characterization close to the sample may be difficult from the practical point of view, the beam path to the FROG spectrometer will be made identical (in terms of dispersion) as the path to the sample.

6.2 Laser–vacuum coupling system

The laser is coupled into the AQS and NQS experiment chambers within a laser in-coupling chamber (LIC) (Figure 6.2) sited right upstream the AQS/NQS entrance flange (Figure 3.1.5). This chamber is part of the

KB–AQS coupling assembly, including the differential vacuum chamber and beam baffling system, for which the design is currently under development.

The LIC hosts the last OL mirror steering the beam towards the interaction point, held by an Allen-key driven mount for sake of rigidity, and two sets of four blades for X-ray and OL beam baffling purposes. Depending on the specific application, the OL mirror may be mounted in such a way that the laser and the X-ray beam are collinear or quasi-collinear (not shown in Figure 6.2). The mirror holder system will be designed in such a way that it is compatible with both solutions.
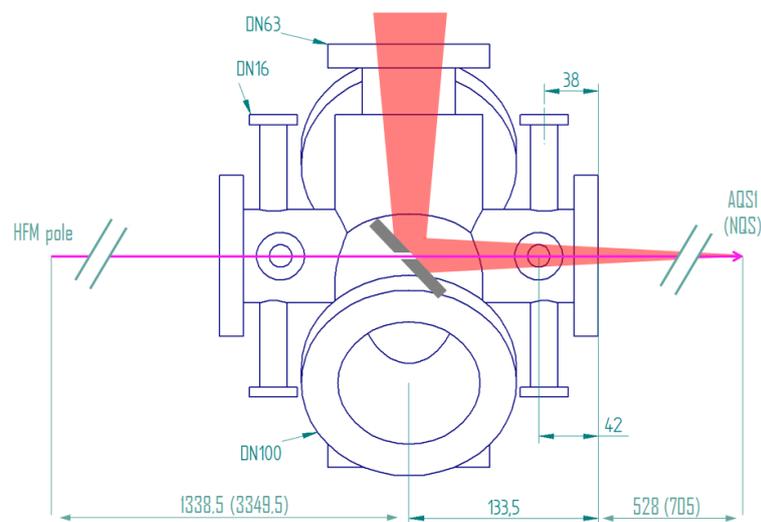
Figure 6.2: *Sketch of the laser in-coupling chamber (LIC) including distances between last KB mirror pole, in-coupling mirror, and interaction point for the AQS (NQS) chamber. Besides the OL coupling, the vessel hosts two sets of four motorized blades for beam baffling.*

In the first case, the OL mirror has an axial hole to let the FEL beam through. Given the distances shown in Figure 6.2 and the clear aperture of the KB mirrors (7.8 x 7.8 mm), the maximum FEL beam spot size is 1.9 x 2.6 mm (1.35 x 1.60 mm) in the mirror position in the AQS (NQS) LIC. Assuming a Gaussian profile for the OL beam, with a 2.7 mm diameter hole in the centre of the mirror (which is reflecting at 45°), a footprint ($1/e^2$) of 40.4 (122.2) mm is (would be) needed for having a transmission of 85% (95%) for the OL. A 2" standard is therefore a reasonable compromise for the holed mirror design. With a 40 mm $1/e^2$ footprint and the OL mirror interaction point

distances indicated in Figure 6.2, the obtained *f*-number gives a FWHM spot size for 800 nm of 28.1 (35.7) µm in the F1 (F2) interaction region. This in-coupling configuration might not be suited to experiments where a much larger spot size is needed, because, if the OL focusing lens/mirror is detuned to get a larger spot size, the hole in the mirror is imaged in the interaction region giving the characteristic donut-like shape. Increasing the spot size by increasing the *f*-number (decreasing the footprint size) would on the other side affect the beam transmission and eventually increase the spot shape distortion caused by far-field effects. A smaller hole would yet be suitable for the in-coupling in the NQS chamber or for higher photon energies, relaxing these constraints somewhat.

Alternatively, the mirror can be set in such a way that the FEL and the OL beam do not enter collinearly into the interaction region. This solution is less straightforward in terms of FEL–OL beams aligning procedure, but allows tuning of the OL footprint on the mirror and therefore of the *f*-number without problems of focal shape distortion and loss in OL intensity. For sake of exemplification, a relative angle of 2.2° (1.0°, 0.5°) is the minimum needed for reflecting the whole $1/e^2$ footprint needed for a 20 (50, 100) µm $1/e^2$ spot size in the F1 (AQS) interaction region.

The last set of blades cannot baffle the FEL beam without interfering with the OL. One possibility under consideration is to have this set of blades made out of a material transparent to IR (e.g. glass). Care must be taken in the design to minimize the impact on the OL pulse time shape caused by a possible non-uniform optical path length over the beam section, which would be introduced by this solution. The up-chirping compressor setting should also be optimized to compensate the dispersion introduced by this additional element.

7 FEL beam diagnostics

A set of diagnostics devices is available at the SQS scientific instrument. Design, installation, and test of the equipment will be done in close collaboration with the X-Ray Photon Diagnostics group (WP74) in order to ensure, if possible, similar standards for all scientific instruments at the European XFEL facility. It is envisaged to provide "online" diagnostics for the main FEL parameters, whenever possible, on a pulse-to-pulse basis, i.e. at the repetition rate of 4.5 MHz of the European XFEL. Triggered by the availability of the X-ray FELs in the US (LCLS) and in Japan (SACLA), there has been an intense activity during the last years to develop new tools with increasing precision and performances. It is expected that this situation will further improve in the near future, since there is a strong demand to characterize most of the FEL parameters for each individual pulse, and for the European XFEL at high repetition rate. The new developments will be monitored and possible improvements to the present design will be incorporated, whenever possible and adequate.

The following photon beam parameters can be provided "online" and will be integrated directly in the data acquisition system:

7.1 Wavelength resp. photon energy

The wavelength of the FEL radiation can be monitored by each of the two spectrometers installed in the AQS chamber around the F1' focal point, i.e. the XUV fluorescence spectrometer and the MBES (see Chapter 3.2.1). Both spectrometers can be used for diagnostics on the extended beam (at the F1' focus position), when the experiments are performed on the focused beam either in the primary focus of AQS (F1) or in the NQS (F2) chamber. The minimal focus in F1 (F2) corresponds to a beam diameter of about 1.5 (4) mm in F1'.

Monitoring the photoemission from an appropriate electron subshell in a rare-gas atom with the MBES provides a direct determination of the mean photon energy of the FEL pulses. A resolution of 10^4 of the electron spectrometer is envisaged, which is much larger than the bandwidth of the ionizing FEL radiation (0.5%). The electron spectra are recorded and stored with the 4.5 MHz repetition rate. When recorded in parallel with the actual experiment, the electron spectra will permit us to monitor, with high precision, relative changes of the photon energy on a single-shot basis. For the determination of the absolute value of the photon energy, a careful normalization procedure has to be undertaken at the beginning of a measuring period.

Similarly, the XUV spectrometer is able to provide an energy resolution of 10^4. A small portion of the FEL beam has to be intercepted and directed towards the spectrometer. The intensity of the deflected photons should be high enough to perform measurements for a single FEL pulse. In addition, it is envisaged to use a detector system and a readout electronics for the XUV spectrometer that is compatible with the 4.5 MHz operation mode of the European XFEL.

7.2   Pulse energy

An X-ray gas monitor detector (XGMD) will be developed for the application at the European XFEL [XFEL-Internal report, 2011]. Similar to the GMD used at FLASH [e.g. Richter et al., APL 83, 2970 (2003)], the detection principle is based on the atomic photoionization of the rare-gas target (Figure 7.1). The detector should operate at relatively low pressure in the range of 10^{-6} to 10^{-4} mbar in order to avoid space charge effects and secondary ionization processes within the gas, and thus provide a required temporal resolution better than 200 ns for online indestructible pulse-resolved measurements of the photon flux. The detector will be able to operate in the broad photon energy range from 250 eV up to 12.4 keV (or at even higher energies) with an absolute uncertainty less than 10% for intensity determination and a relative standard uncertainty for pulse-to-pulse intensity instabilities of 1% for more than 10^{10} photons per pulse.
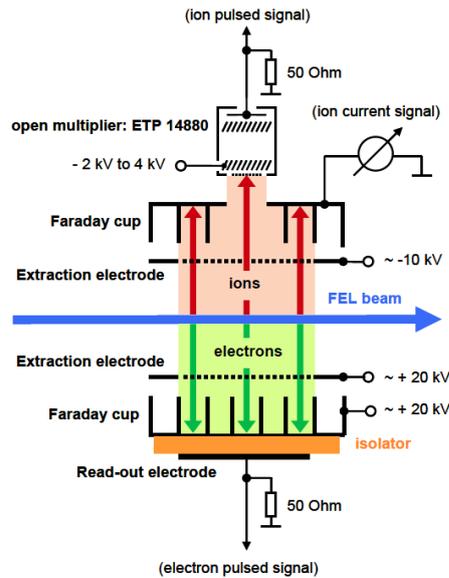
Figure 7.1: Schematic diagram for the XGMD used at the SQS scientific instrument

The XGMD will be installed in front of the KB mirror system to monitor on a single-shot basis the intensity delivered to the experiment station, i.e. after having passed all optical components such as off-set mirrors, apertures, and (optional) the soft X-ray monochromator.
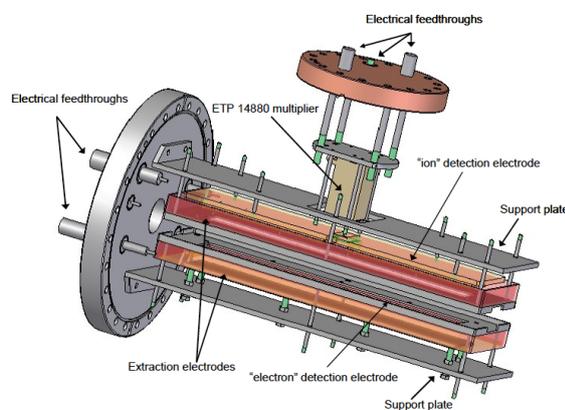
Figure 7.2: Technical design for the XGMD used at the SQS scientific instrument

The present technical layout for the XGMD foresees a distance between the electrodes used for the electron and ion detection of 2 cm. This value will determine the final place for the installation of the XGMD on the beamline, since the beam diameter in the soft X-ray regime (< 500 eV) can be larger than 5 mm (FWHM).

7.3   Pulse arrival time

Timing diagnostic techniques aim at characterizing the arrival time and possibly the temporal shape of the FEL pulse. Different encoding techniques for the time structure of the pulse are presently under development at FLASH and at the LCLS and might be integrated in the SQS instrument. The working principle, the current status of attainable resolution and dynamic range, and the compatibility with high repetition rate (MHz) single-shot characterization are briefly discussed here for three selected techniques, together with a tentative scheme for their setup within the SQS experiment layout.

The techniques presented here measure the arrival time of the FEL pulse with respect to an external clock given by the experiment-dedicated optical laser. This feature is perfectly fitting with their main purpose, as for time-resolved pump–probe experiments the precise knowledge of the relative timing of the FEL and the optical laser is a main requirement.

The integration of the described techniques within the SQS layout is intrinsically invasive for the FEL beam, so that they must be set up in the diagnostics chambers downstream the experiment station.

7.3.1   Spectral encoding

The spectral-encoding technique makes use of X-ray induced fast changes in the dielectric function of a membrane to map the relative delay between the FEL beam and an optical laser onto a spectral coordinate [Bionta et al., Opt. Exp 22, 21855 (2011)].

A broadband laser pulse is chirped so that the different frequency components of the optical pulse reach the interaction point at different times. Amplitude modulations, like e.g. a step function applied in the time domain, are thus linearly mapped into the spectral distribution. In this way, the rising edge of the temporal modulation of the transmission function of a membrane produced by the X-ray interaction can be manifested as a rising edge in the laser-transmitted spectrum through the membrane itself.

The resolution and dynamic range of this technique are basically determined by the spectral chirp parameter. Decreasing the chirp reduces the temporal window, improving the resolution and providing a simple way to zoom on the temporal feature of interest. At present, this technique can measure the arrival time of an FEL pulse with a ~25 fs RMS resolution within a 3 ps temporal window [Bionta et al., 2011].
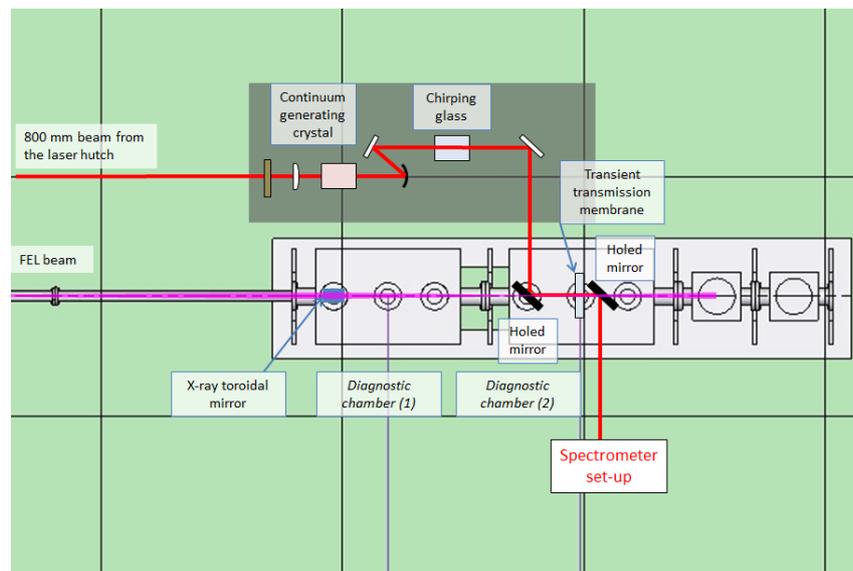
Figure 7.3: Tentative schematic layout for the spectral-encoding setup at the SQS end station [adapted from Bionta et al., 2011]. The setup is installed in the two diagnostics chambers downstream the end station (see Figure 7.5). Due to the high divergence of the FEL beam, the possibility of refocusing is foreseen. The relative position of the refocusing mirror, the two holed OL mirrors and the transient-transmission membrane can be adjusted to optimal operation conditions.

A possible layout for integrating a spectral-encoder system in the SQS experiment station is shown in Figure 7.3. Two main issues are to be addressed before the technique can be employed at the European XFEL:

1 The high intra-burst repetition rate will possibly cause a sensible thermal load on the transient-transmission membrane, eventually modifying its optical properties in an uncontrolled way and possibly destroying it. The use of a Si_3N_4 membrane, as done by Bionta et al. (2011), is probably problematic. The principle is yet material-independent and can for instance be developed in reflection geometry, as the installation is foreseen downstream the experiment chamber, involving the use of a

conductor. Alternatively, an optically clear material that is still absorbing the X-rays might be employed.

2 When operating the FEL at high repetition rate, the single-shot characterization is not viable with a standard CCD-based spectrometer. As the measurement requires 1D information, the use of a Gotthard detector is a possible solution.

A more cost-effective solution might involve the use of a piezo-driven motor continuously steering the beam in the direction perpendicular to the spectrometer dispersion during each bunch train. A stage moving approximately 20–50 steps/µs would be able to encode the burst structure into an angular dispersion, so that the 2D capability of the spectrometer camera would be fully exploited for the spectral encoding of the time structure along one direction for a bunch of pulses along the other direction. The maximum number of bunches that can be recorded depends on the number of pixels and on the pixel size of the camera, related to the minimum focal size that can be attained in the entrance of the spectrometer.

## 7.3.2 Spatial encoding based cross-correlator

Spatial encoding also features an X-ray–OL cross-correlator exploiting the transient change in optical properties of a material [Schorb et al., APL100, 121107 (2012)]. In this case, it is the X-ray induced reflectivity change that is used as a marker of the arrival time of the FEL pulse, probed by an optical laser beam.

At present, this technique can provide information about the X-ray–OL time delay with a resolution of 22 fs RMS [Schorb et al., 2012] with a temporal window of 1 ps.

The problematic issues and the perspectives mentioned for the spectral-encoding method are also valid here, as the cross-correlator technique has been developed using the same material featuring transient optical properties and also uses a CCD for detecting the reflected optical laser beam.

7.3.3 Electron energy encoding by superposed streaking field

Commonly known as photoelectron streaking technique, this solution is named electron energy encoding here for the sake of consistency with the other techniques presented. The principle is adapted from attosecond metrology, where a few-cycle IR laser pulse is superposed onto an XUV pulse generated through high-harmonic generation, which is used to eject photoelectrons from a rare-gas target. The superposition causes a broadening and shifting of the initial kinetic-energy distribution of the photoelectrons. If the photoemission process is confined within a much shorter period than the half cycle of the superposed field, the detected photoelectron spectrum is said to be streaked, and the external field encodes the temporal structure of the ionizing pulse in the kinetic-energy distribution of the emitted electrons (Figure 7.4) determined by the vector potential amplitude of the streaking field. In opposition to spectral and spatial encoding, this technique is not limited to characterizing the arrival time, but can provide the users, within the resolving power, with full information about the temporal distribution of the FEL pulse. As the technique is based on electron energy spectroscopy, this diagnostics technique is able to perform shot-to-shot characterization thanks to the specification of the SQS DAQ system.
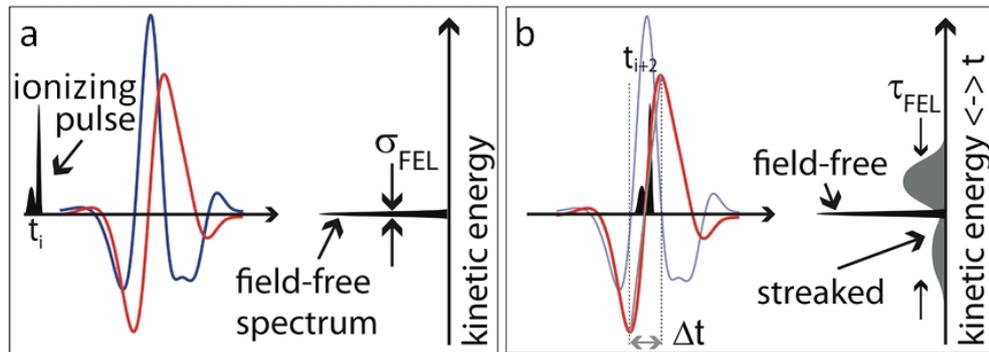
Figure 7.4: *Schematic of electron streaking measurement [adapted from Grguras et al., Nat. Photonics 6, 852 (2012)]. The blue and red curves represent the electric field and corresponding vector potential of a single-cycle THz pulse. In the measurement depicted in (a), the FEL pulse does not overlap in time with the streaking pulse and the kinetic-energy distribution of photoelectrons ejected by the FEL pulse is unaffected. If the induced photoemission overlaps with the streaking field (b), the electron spectrum is encoding the time distribution of the ionizing pulse, getting broadened according to the pulse duration and shifted according to the time of arrival with respect to the streaking pulse.*

The temporal dynamic range of this technique for the pulse duration measurement is intrinsically limited by the half-cycle length of the streaking pulse field; this together with the vector potential amplitude also determines the resolution. A THz streaking field is the solution providing the optimal dynamic range for the needs of the SQS instrument (1 to >100 fs): single-cycle THz pulses can be produced by tilted wavefront generation in a $LiNbO_3$ crystal or by difference frequency generation in an organic crystal [Appl. Phys. Express 1 (2008) 042002], with a half-cycle duration depending on the material used and varying between 250 and 600 fs. For experiments where the machine is operated in low bunch charge mode (few fs pulse duration), an IR streaking field in the range of 10–17 µm wavelength, corresponding to 15–28 fs half-cycle duration, may be suitable. This radiation can be produced by two OPAs operated in difference frequency generation.

The resolution of this technique depends on the combined effect of the streaking-field amplitude, corresponding to the slope of the energy-to-time mapping function given by the vector potential (Figure 7.4), and of the original width of the unstreaked electron energy distribution. The former gets improved when using a more intense or shorter streaking-field pulse, whereas

the latter is affected by the electron spectrometer resolution. For SASE pink FEL beam and for cases where the electrons correspond to a photoline, the width of their original energy distribution in the keV photon energy range gets comparable to the streaking amplitude (typically some tens of eV for a few µJ/pulse THz energy). For this reason, the streaking of Auger lines is to be foreseen in these measurements, since the Auger emission has a given natural width, which can be as small as a few fs (2.6 fs for Ne KVV line). In this way, the measurement resolution can be completely decoupled from the properties of the FEL radiation. For sake of exemplification, with a 120 eV streaking amplitude, 250 fs streaking pulse duration, and 2 eV original electron line width, a resolution of ~3 fs could be attained. The present state of the technique is far from this level, but a strong development effort is ongoing.
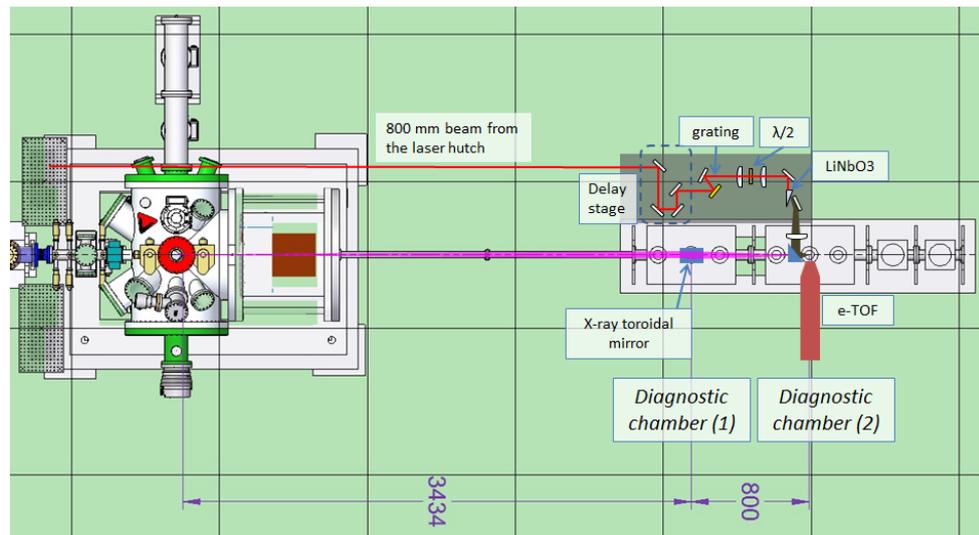
Figure 7.5: *Layout of the electron streaking diagnostic setup in the SQS end station [adapted from Grguras et al., Nat. Photonics 6, 852 (2012)]. The setup is installed in the two diagnostics chambers downstream. The streaking radiation (THz from tilted wavefront generation in LiNbO3 in this representation) is generated close to the chamber. The FEL beam (here coming from the NQS focal point) is refocused by a toroidal mirror, situated in the first chamber, into a 50–100 µm spot in the second chamber. The detailed design for the mirror has still to be defined. The streaking radiation is superposed onto the FEL refocused radiation. The streaked electrons are collected by an eTOF.*

A sketch of the layout for integrating the technique in the SQS experiment station is shown in Figure 7.5. The electron spectrometer needs sub-millimetre spot size for an optimal resolution, so a refocusing stage has to be foreseen in the first diagnostics chamber. A toroidal mirror capable to refocus F1, F1', and F2 with a spot size < 100 µm in an interaction region within the second diagnostics chamber will be designed. The diagnostics chamber will be equipped with an eTOF and a setup for electro-optical sampling aimed at characterizing the THz pulse.

7.4   Position monitor

One possibility to visualize the FEL beam close to the experiment area and to determine the correct beam definition is given by the so-called "pop-in monitors". Their function is described in detail in the CDR "Imaging Stations for Invasive Photon Diagnostics" by C. Ozkan (WP74) [XFEL.EU TR-2012-004]. These detectors are mainly developed for the initial alignment and re-adjustments of optical elements and operate only in single-bunch mode (10 Hz), but they can also be used as a beam position monitor in the experiment area.

The pop-in monitors enable the determination, from the recorded images, of the centre of mass, the intensity, and the width of the FEL beam at a certain position. The area should be large enough to cover the possible range of beam displacements. The minimum diameter of the scintillator screens should therefore be larger than the alignment tolerance. The screen can be made from Ce:YAG allowing to provide large active areas.

The conceptual design of such an imaging station is shown in Figure 7.6.
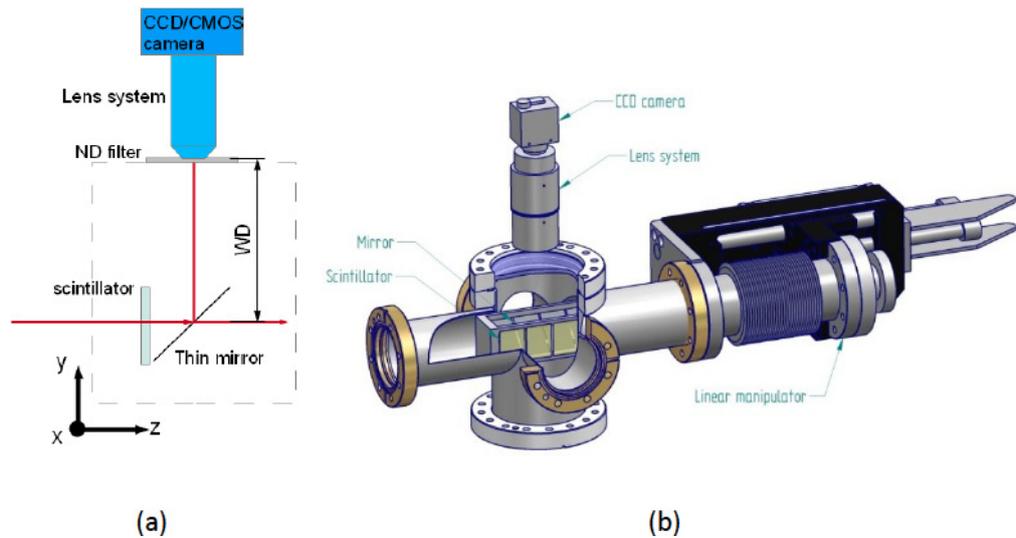
Figure 7.6: *(a) Optical imaging system and (b) mechanical model for the imaging station [from CDR (WP74): Imaging Stations for Invasive Diagnostics].*

The limiting parameter for this device, preventing it to operate in the 4.5 MHz mode, is the readout camera, which should provide a large sensing area, high sensitivity, large dynamical range, and a low noise level.

8   Add-on equipment

1   **Ion storage ring:**

A proposal for the installation of an ion storage ring is promoted by
H. Pedersen (Aarhus), A. Wolf, and J. Crespo (Heidelberg). The
collaboration suggests a permanent installation of an ion storage ring
(2.7×4.4 m^2) into the SASE3 beamline. The storage ring could be used in
parasitic mode and would be transparent for other users. A possible
installation could be at the open port.

2   **X-ray crystal fluorescence spectrometer:**

For experimental studies using high-resolution fluorescence spectroscopy
in the photon energy range above 1.5 keV, which is not covered by the
VLS spectrometer described above, the use of a crystal monochromator
similar to the one described by Journel et al. [Rev. Sci. Instrum. 80,
093105 (2009)] could be envisaged. A French user consortium (M. Simon,
LCPMR, Paris) could provide this type of spectrometer for the SQS
instrument.

3   **Cluster source:**

A cluster source dedicated to various cluster types is under development
by a user consortium (T. Möller, TU Berlin). The final layout will be done in
close discussion with the user group in order to assure compatibility with
other equipment at the AQS and NQS experiment chambers and to
integrate, if possible, any specific space requirement.

9   Timeline

The timeline for the design, construction, test, and installation of the different components is mainly determined by two boundary conditions. First, access to the experiment hall will be given only in summer 2015; second, the first beam at the SASE3 beamline is expected for the beginning of 2016. Therefore, the second half of 2015 will be completely dedicated to the installation and pre-testing of *all* equipment belonging to the SQS scientific instrument.

In addition, the final definition of parameters for the spectrometers is still continuing in discussion with the interested user community. For each spectrometer, an individual test and installation phase can be scheduled depending on its complexity and the already acquired expertise with this type of spectrometer. With respect to laser and diagnostic devices, the final definition will be as late as possible, since the last developments should be taken into account for the installation phase.

Special consideration will be given to the KB optics, which certainly requires a long time of delivery (about two years). A possible scenario for the timeline is given in Table 9.1.

Similarly, the envisaged schedules for the installation of the AQS and NQS experiment chambers are presented in Tables 9.2 and 9.3.

Table 9.1: *Timeline for the design and installation of the KB optics*

	2012	2013				2014				2015				2016	
	4. Quarter	1.	2.	3.	4.	1.	2.	3.	4.	1.	2.	3.	4.	1.	2.
Simulations	■	■													
Final definition of mirror design		■	■												
Design of mirror chamber		■	■												
Call for tender			■												
Purchase order				■	→										
Reception of material											■				
Installation of material												■			
Test and commissioning													■	■	

Table 9.2: Timeline for the design, assembly, test, and installation of the AQS chamber

	2012	2013				2014				2015				2016	
	4. Quarter	1.	2.	3.	4.	1.	2.	3.	4.	1.	2.	3.	4.	1.	2.
Chamber mechanics	Final design			Purchase and reception					Assembly Lab. HH			Installation XFEL&Test		FEL commissioning	
Chamber vacuum	Final design			Purchase and reception					Assembly Lab. HH			Installation XFEL&Test		FEL commissioning	
Diff. Pump.			Final design			Purchase and reception			Assembly Lab. HH			Installation XFEL&Test		FEL commissioning	
Opt. Laser components	Definition of parameters (I)		Test in Lab. HH			Definition of parameters (II)			Test in Lab. HH			Installation XFEL&Test			
HReTOF	Parameter optimization		Fabrication			Assembly & Test						Installation XFEL		FEL commissioning	
VMI	Final design			Fabrication			Assembly & Test			Test in Lab. HH		Installation XFEL		FEL commissioning	
MBES (Uppsala)	Design		Fabrication			Test in Uppsala		Installation Lab. HH		Test in Lab. HH		Installation XFEL		FEL commissioning	
XUV spectrometer (Uppsala)	Design		Fabrication			Assembly HH				Test in Lab.HH		Installation XFEL		FEL commissioning	

Table 9.3: *Timeline for the design, assembly, test, and installation of the NQS chamber*

	2012	2013				2014				2015				2016	
	4. Quarter	1.	2.	3.	4.	1.	2.	3.	4.	1.	2.	3.	4.	1.	2.
Chamber mechanics		Final design			Purchase and reception					Assembly Lab. HH		Installation XFEL&Test			
Chamber vacuum		Final design			Purchase and reception					Assembly Lab. HH		Installation XFEL&Test			
Diff. Pump.				Final design			Purchase and reception			Assembly Lab. HH		Installation XFEL&Test			
Opt. Laser components	Definition of parameters (I)		Test in Lab. HH			Definition of parameters (II)		Test in Lab. HH				Installation XFEL&Test			
REMI	Parameter optimization			Fabrication		Assembly & Test in Lab. HH						Installation XFEL		FEL commissioning	
eTOF	Final design				Fabrication			Assembly & Test in Lab. HH				Installation XFEL		FEL commissioning	
Thomson Parabola				Design		Fabrication		Assembly & Test in Lab. HH				Installation XFEL		FEL commissioning	
Imaging detector	Definition of parameters		Purchase and reception							Test in Lab.HH		Installation XFEL		FEL commissioning	

10   Acknowledgements

For the writing of many chapters, we acknowledge substantial support and various contributions from other work packages, in particular:

WP73 X-Ray Optics and Beam Transport: Harald Sinn, Daniele La Civita, and Liubov Samoylova

WP75 Detector Development: Markus Kuster and Monica Turcato

WP76 DAQ and Control Systems: Chris Youngman, Nicola Coppola, and Patrick Gessler

WP79 Sample Environment: Joachim Schulz und Sadia Bari

WP74 X-Ray Photon Diagnostics: Jan Grünert

WP78 Optical Lasers: Max Lederer

Photon System Coordination: Tobias Haas

Thanks also to the scientific directors for the European XFEL, Serguei Molodtsov and Thomas Tschentscher, as well as to the instrument scientists Christian Bressler, Anders Madsen, Adrian Mancuso, and Andreas Scherz.

In addition, we acknowledge very helpful discussions and suggestions from Adrian Cavalieri, Ryan Coffee, Raimund Feifel, Markus Ilchen, Thomas Möller, Joseph Nordgren, Lorenzo Raimondi, Jan-Erik Rubensson, Riccardo Signorato, and Jens Viefhaus.